BINARY DETECTION USING MULTI-HYPOTHESIS LOG-LIKELIHOOD, IMAGE PROCESSING

THESIS

Brent H. Gessel, Captain, USAF

AFIT-ENG-14-M-34

DEPARTMENT OF THE AIR FORCE
AIR UNIVERSITY

AIR FORCE INSTITUTE OF TECHNOLOGY

Wright-Patterson Air Force Base, Ohio

BINARY DETECTION USING MULTI-HYPOTHESIS LOG-LIKELIHOOD,

IMAGE PROCESSING

THESIS

Presented to the Faculty

Department of Electrical and Computer Engineering

Graduate School of Engineering and Management

Air Force Institute of Technology

Air University

Air Education and Training Command

in Partial Fulfillment of the Requirements for the

Degree of Master of Science in Electrical Engineering

Brent H. Gessel, B.S.E.E.

Captain, USAF

March 2014

AFIT-ENG-14-M-34

BINARY DETECTION USING MULTI-HYPOTHESIS LOG-LIKELIHOOD,

IMAGE PROCESSING

Brent H. Gessel, B.S.E.E.
Captain, USAF

Approved:

//signed//	20 Feb 2014
Stephen C. Cain, PhD (Chairman)	Date
//signed//	13 Feb 2014
Keith T. Knox, PhD (Member)	Date
//signed//	20 Feb 2014
Mark E. Oxley, PhD (Member)	Date

AFIT-ENG-14-M-34

Abstract

One of the United States Air Force missions is to track space objects. Finding planets, stars, and other natural and synthetic objects are all impacted by how well the tools of measurement can distinguish between these objects when they are in close proximity. In astronomy, the term *binary* commonly refers to two closely spaced objects. *Splitting* a binary occurs when two objects are successfully detected. The physics of light, atmospheric distortion, and measurement imperfections can make binary detection a challenge.

Binary detection using various post processing techniques can significantly increase the probability of detection. This paper explores the potential of using a multi-hypothesis approach. Each hypothesis assumes one two or no points exists in a given image. The log-likelihood of each hypothesis are compared to obtain detection results. Both simulated and measured data are used to demonstrate performance with various amounts of atmosphere, and signal to noise ratios. Initial results show a significant improvement when compared to a detection via imaging by correlation. More work exists to compare this technique to other binary detection algorithms and to explore cluster detection.

Table of Contents

List of Figures

List of Tables

List of Acronyms

Acronym   Definition

CCD Charge-Coupled Device

P_D Probability of Detection

P_{fa} Probability of False Alarm

PSF Point Spread Function

OTF Optical Transfer Function

FT Fourier Transform

PSD Power Spectral Density

LiDAR Light Detection And Ranging

PMF Probability Mass Function

SST Space Surveillance Telescope

DARPA Defense Advanced Research Projects Agency

GEO Geostationary Earth Orbit

BINARY DETECTION USING MULTI-HYPOTHESIS LOG-LIKELIHOOD,

IMAGE PROCESSING

I. Introduction

COMPARING statistical hypotheses to determine the likelihood of a given event is a proven technique used in many fields, particularly digital communication. The application of a multi-hypothesis test algorithm to the detection of binary stars or other space objects is an area of new exploration. This thesis will explore the usefulness of using a multi-hypothesis technique to resolve close binary objects in space. The first task is to derive a multi-hypothesis algorithm specifically for binary detection and then provide results for various simulated imaging conditions as well as measured binary images. Simulated results will be compared with another technique to explore potential detection improvements.

1.1 Binary detection

The ability to discriminate between closely-spaced objects in space has and continues to be a challenge. Finding planets, stars, and other natural celestial objects, as well as trying to keep track of satellites and space debris are all impacted by how well the tools of measurement can distinguish between these objects in close proximity. In astronomy, the term *binary* commonly refers to two stars in the same system. *Splitting* a binary occurs when two stars are successfully identified. Some binaries are easily split using basic equipment. As the source intensity, object distance, and/or atmospheric distortion varies, the binaries will appear as just a single object. In this paper, the term *binary* refers to any two closely spaced objects. Several image post processing techniques have been developed

to increase spatial resolution and/or look for patterns common to binary objects. Most of the commonly used methods today focus on image reconstruction and deblurring. This thesis will show that if an image's Point Spread Function (PSF) is known and the source is a single or double point source, the log-likelihood of the most probable hypothesis provides a statistical comparison of how likely a blurred image contains a binary.

1.2 Space situational awareness

One of the United States Air Force missions is to track space objects, particularly of the synthetic kind. Due to the physics of spatial resolution, it is extremely difficult to resolve satellites in geosynchronous orbit (35,786 km). At this distance the size of a satellite is typically smaller than one pixel on a high quality Charge-Coupled Device (CCD) camera. For example, if a satellite in geosynchronous orbit is 15 meters wide (the length of a full size school bus) and a telescope with an aperture of 4 meters and focal length of 64 meters is focused on it, the size on the CCD would be:

$$size = \frac{(sat.size)(focal.length)}{distance} = \frac{(15m)(64m)}{35,786,000m} = 2.64\mu m. \tag{1.1}$$

This is much smaller than a typical CCD pixel used in astronomical telescopes. This is also smaller than the Raleigh criteria for spatial resolution for this same setup [14]:

$$Resolution \approx (1.22)(\lambda)(f/\#) = (1.22)(550nm)(16) = 8.48\mu m \tag{1.2}$$

where λ is the wavelength of light and $f/\#$ is the f-number, which is the focal length divided by the diameter of the optical system. The atmosphere will further blur this image and after a certain amount of exposure time the image will typically be a few to several pixels of light. At this distance, it can be extremely difficult to tell if there is one, two or several objects in the spot of light.

The multi-hypothesis method discussed in this thesis has the potential to increase the probability of correctly detecting binaries at geosynchronous orbit and other scenarios important to the USAF.

1.3   Research objectives

The question posed in this thesis is how well, if at all, can a multi-hypothesis model correctly detect a binary pair in a blurred image? To answer that question four research objectives are documented.

First, a statistical model is derived in Section 3.1. Here the derivation of algorithms for zero, one, and two point sources are shown.

The second objective is to successfully implement the mathematical algorithms into a software simulation model. This model includes atmospheric effects, background noise, and creates a test environment to work out threshold parameters that maximize the probability of detection while minimizing the false alarm rate. The simulation will be done in Matlab™and is covered in Section 3.2.

Once the binary hypothesis method is successfully implemented and results measured, it is important to compare them to another modern technique. The third objective is to compare results from another image detection method, specifically imaging by correlation with a threshold set for binary detection. Section 3.3 walks through an implementation of imaging by correlation in Matlab™and results are provided in Chapter 4.

The final objective is to use measured imagery data where the number of objects is known and see how well the algorithm correctly detects when a binary is present. The imagery data used is focused on a satellite in geosynchronous orbit with a dim star passing by at various distances, including the situation where the two appear as a single object. The decision to select a binary from the algorithm is compared against the truth data and presented in Chapter 4.

1.4   Organization

This research document is organized in accordance with AFIT's thesis guidelines. Chapter 2 will discuss current methods used to detect binaries and contrast them with the proposed, unpublished, multi-hypothesis binary detection method. Chapter 3 provides the

derivation and simulation methods used to meet the thesis objectives outlined in the previous section. Chapter 4 contains the results of several of the simulation tests as well as the results of processing measured data. Chapter 5 discusses conclusions and opportunities for continued research and operational testing. Complete references of all sources cited are contained in the bibliography. Every attempt has been made to use consistent variables to enhance readability.

II.   Background

Hᴵᴳʜ spatial resolution of an imaging system is key to achieving detection of binary objects. A standard telescope system cannot achieve diffraction-limited resolution due to factors such as atmospheric and optical aberration. Several techniques have been developed to close the gap between diffraction-limited resolution and a system's actual resolution. This chapter will discuss some of the most common post-processing techniques to increase spatial resolution in astronomical imaging. Additionally, a brief overview of multi-hypothesis statistics is provided.

Binary objects do not all behave in the same way. Although the imaging techniques discussed in this chapter can be used on all binaries, specific methods have been developed to look for planets and binary star systems. As gravitational fields of large planets and stars interact, a periodic movement, often referred to as *wobble*, can be detected [23]. Other indicators such as periodic eclipsing and Doppler-like wavelength patterns can infer the presence of a binary [6]. These methods have been successful on a subset of binaries but cannot be applied to binaries in general. This paper will not focus on gravitational, orbital or other spectroscopic measurements techniques, rather the focus will be on post-processing techniques useful in detecting any binary.

Aside from the natural effect of diffraction, the earth's atmosphere plays a large role in limiting spatial resolution. Virtually all real-time and post-processing de-blurring techniques require an understanding of how the atmosphere is changing the light. Because we know what a diffraction-limited point source looks like, we can compare it to a measured point source through the same atmosphere and use that information to correct the atmospheric distortion [14][12]. Lightwaves from distant point source(s) can be estimated as plane waves right before reaching earth's atmosphere [14]. The atmosphere will randomly distort this wave and the distortion can be measured by a wavefront sensor

[33]. Unfortunately, it is impossible to have a perfect natural point source everywhere in the night sky at visible wavelengths [11][37][38][39]. To overcome this limitation, one or more lasers can be used to create point sources, or guide beacons, in the area of interest [7][9][10][11][15][37]. A wavefront sensor takes the point source, or guide star, information and determines corrective adjustments then sends that data to an adaptive optics system [32]. Real world performance of adaptive optics can vary from near diffraction limited correction to no visible improvement depending on a host of factors [1][8][16][17][28][36][40].

The need for a valid point source cannot be understated since it is foundational to adaptive optics and the post-processing techniques described in this chapter. A great deal of research still remains in the field of generating and measuring quality point sources. Although adaptive optics is an important technique in moving closer to diffraction limited imaging, it is not currently a practical solution for all imaging sites. Having one or more image post-processing software solutions is a relatively affordable way to augment or supplement adaptive optic systems. It is the area of software post-processing that this paper will focus from this point on.

The following sections will discuss two of the most common post-processing methods for binary detection, deconvolution and speckle interferometry. Section 2.2 finishes the chapter with a brief and general look at how multi-hypothesis statistics can be used in binary detection.

POINT SOURCE

LIGHTWAVES

RANDOM ATMOSPHERIC TURBULENCE

TELESCOPE

BEAM SPLITTER

CCD

ADAPTIVE MIRROR

WAVEFRONT
SENSOR

MIRROR CONTROL
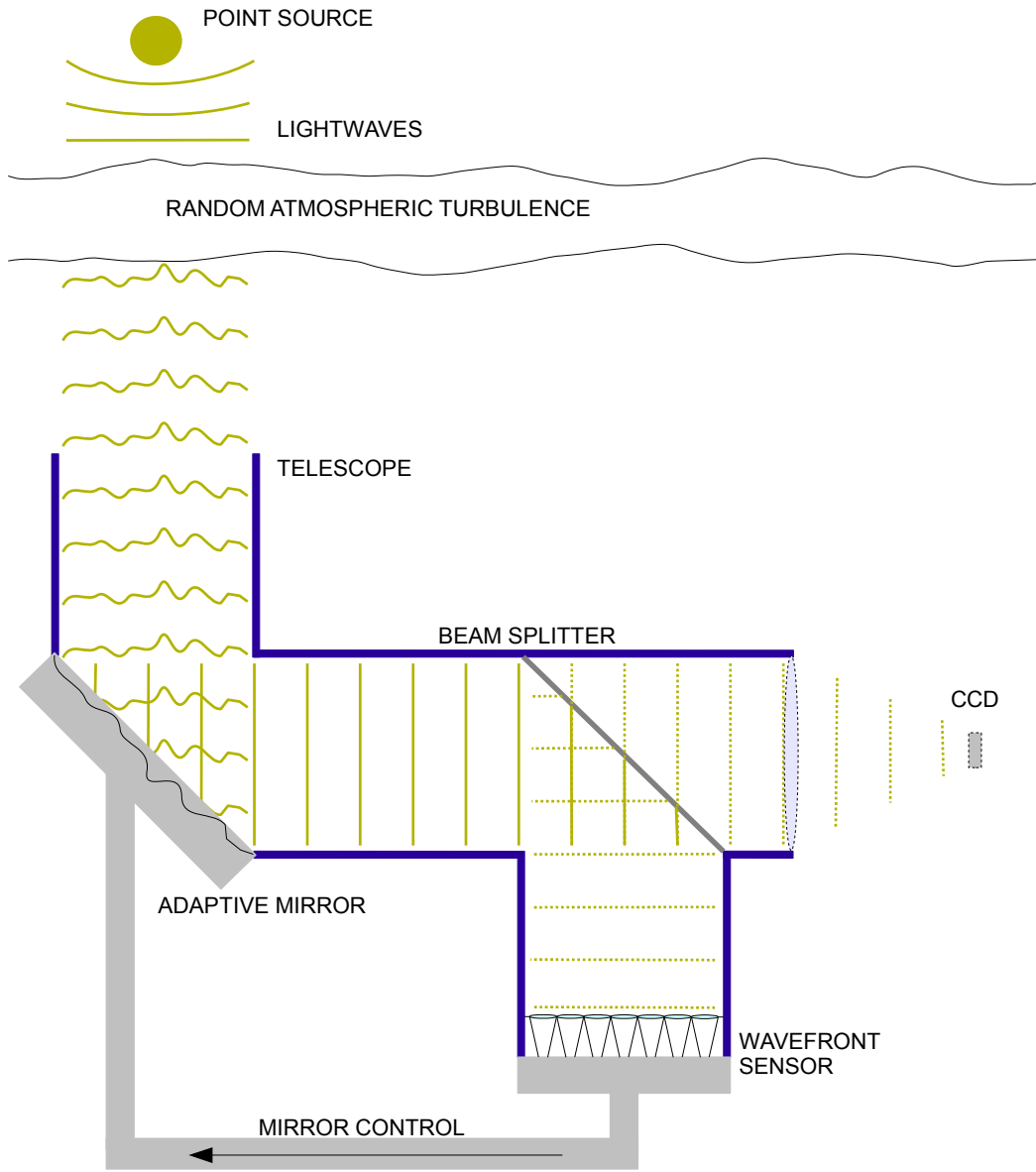
Figure 2.1: Basic adaptive optic process.

2.1 Post-Process Imaging

Image post-processing can be an effective and affordable way to increase image resolution. This section will look at two deconvolution methods and a speckle interferometry technique useful for visual binary detection. These processes attempt to reconstruct a higher resolution image from measured data. It is important to note that the multi-hypothesis method does not produce a reconstructed image so it is a fundamentally different approach but still fits within the post-processing category of binary detection.

2.1.1 Atmospheric Turbulence.

Before discussing specific imaging techniques it is important to explain how atmospheric turbulence is modeled in this thesis. The most common methods utilize the approximation that atmospheric effects can be represented as wavefront errors in the pupil plane. If $A(u, v)$ represents the two-dimensional, clear pupil and $W(u, v)$ represents wavefront error as a function of position with respect to a fixed Cartesian coordinate system, (u, v), then the atmospherically blurred image, $i(x, y)$, can be represented as:

$$i(x, y) = \left| \mathcal{F} \left\{ A(u, v) e^{jW(u,v)} \right\} \right|^2 \tag{2.1}$$

where $\mathcal{F}$ is the symbol denoting the Fourier Transform. The wavefront error as a function of position, commonly called a phase screen, can be simulated in various ways. One of the most common methods of phase screen generation utilizes Power Spectral Density (PSD) models, such as von Kármán and modified von Kármán [31]. These are referred to as Fourier Transform (FT) based methods [31]. The model used in the simulations of this paper are based upon another method that uses Zernike polynomials to generate phase screens.

It has been shown that the wavefront error, $W(u, v)$, can be expanded with basis functions based on the geometry of the aperture [33]. Common basis functions include, Zernike circular, Zernike annular, Gaussian-circular, and Gaussian-annular. A Zernike circular set of basis functions were used in this paper to match the geometry of the

simulated aperture. Expansion of the wavefront error, or phase screen, using Zernike circular polynomials is described below. Note the shift to polar coordinates where, $\rho = \sqrt{u^2 + v^2}$ and θ =arctangent(u, v), also note u and v represent grid locations in the pupil plane. Zernike expansion equations are as follows:

$$W(u, v) = W_z(\rho, \theta) = \sum_i \alpha_i Z_i(\rho, \theta)$$

$$Z_i(\rho, \theta) = \begin{cases} \sqrt{2(n+1)} R_n^m(\rho) G^m(\theta) & \text{if } m \neq 0 \\ R_n^0(\rho) & \text{if } m = 0 \end{cases}$$

$$R_n^m(\rho) = \sum_{s=0}^{(n-m)/2} \frac{(-1)^s (n-s)!}{s!(\frac{n+m}{2} - s)!(\frac{n-m}{2})!} \rho^{n-2s}$$

$$G^m(\theta) = \begin{cases} \sin(m\theta) & \text{if } i\, odd \\ \cos(m\theta) & \text{if } i\, even \end{cases}$$

(2.2)

where combinations of the index variables m and n will produce a specific aberration effect, also the index i is a numerical index. Table 2.1 below shows the mapping of the first 10 Zernike circular polynomials and the index mapping of m, n, and the numerical index, i.

The wavefront error, $W(\rho, \theta)$ can be measured or simulated. It is worth repeating that the wavefront error is using Zernike polynomials:

$$W_z(\rho, \theta) = \sum_i \alpha_i Z_i(\rho, \theta). \tag{2.3}$$

To simulate phase screens we need to generate the coefficients, α_i, to weight each polynomial at a given polar coordinate, ρ, θ. To do this the work of Roddier was utilized, who demonstrated that by using a Cholesky decomposition of the covariance matrix of the Zernike coefficients, statistically accurate atmospheric phase screens can be generated [30]. The following discussion will provide a basic explanation of this method.

First we note that α in Equation 2.3 will be an $N \times 1$ vector where N is the number of Zernike polynomials used to form the basis. Given the covariance matrix, $C_{i,j}$, for two Zernike polynomials and associated amplitudes, α_i and α_j:

Table 2.1: First 10 Zernike Circular Polynomials [33].

i	m	n	$Z_n^m(\rho, \theta)$	Name
1	0	0	1	piston
2	1	1	$2\rho\cos(\theta)$	x tilt
3	1	1	$2\rho\sin(\theta)$	y tilt
4	0	2	$\sqrt{3}(2\rho^2 - 1)$	defocus
5	2	2	$\sqrt{6}\rho^2\sin(2\theta)$	y primary astigmatism
6	2	2	$\sqrt{6}\rho^2\cos(2\theta)$	x primary astigmatism
7	1	3	$\sqrt{8}(3\rho^3 - 2\rho)\sin(\theta)$	y primary coma
8	1	3	$\sqrt{8}(3\rho^3 - 2\rho)\cos(\theta)$	x primary coma
9	3	3	$\sqrt{8}\rho^3\sin(3\theta)$	y primary trefoil
10	3	3	$\sqrt{8}\rho^3\cos(3\theta)$	x primary trefoil
11	0	4	$\sqrt{5}(6\rho^4 - 6\rho^2 + 1)$	x primary spherical

$$C_{i,j} = E[\alpha_i, \alpha_j] \tag{2.4}$$

$$C = L\overline{L^T} \tag{2.5}$$

where $\overline{L^T}$ denotes the conjugate transpose of the lower triangular matrix L. The covariance matrix generated from two Zernike polynomials Z_i and Z_j has been derived by Knoll [27][30]:

$$C_{i,j} = E[\alpha_i, \alpha_j] = \frac{K_{Z_i Z_j}\delta_Z\Gamma[(n_i + n_j - 5/3)/2](D/r_0)^{5/3}}{\Gamma[(n_i - n_j - 17/3)/2]\Gamma[(n_i - n_j - 17/3)2]\Gamma[(n_i - n_j - 23/3)/2]} \tag{2.6}$$

where:

$$K_{Z_i Z_j} = \frac{\Gamma(14/3)[(24/5)\Gamma(6/5)]^{5/6}[\Gamma(11/6)]^2}{2\pi^2} \times (-1)^{(n_i + n_j - 2m_i)/2}\sqrt{(n_i + 1)(n_j + 1)} \tag{2.7}$$

and:

$$\delta_Z = [(m_i = m_j)]\bigwedge[\overline{parity(i, j)} \vee (m_i = 0)]. \tag{2.8}$$

10

If we generate a vector of zero mean with unit variance uncorrelated numbers, **n**, then we can solve for the amplitudes, α, that weight each Zernike polynomial by applying the properties of the Cholesky decomposition such that:

$$L = C^{\frac{1}{2}} \tag{2.9}$$

and:

$$\alpha = L\mathbf{n}. \tag{2.10}$$

Thus, given a randomly generated zero mean, unit variance vector **n**, the Freid seeing parameter, r_0, the diameter of the aperture, D, and the number of Zernike polynomials desired, a wavefront error phase screen can be calculated. Again, this is the method used in all simulation conducted as part of this thesis. For more information on this method please refer to [30].

2.1.2 Deconvolution.

Deconvolution is a de-blurring technique widely used in many fields including astrophotography. Basically, if an image is distorted with spatially invariant blur, e.g. the same atmospheric distortion is applied to the entire image, it can be modeled as the convolution of the measured point spread function and the true image [19]. Or, using the Convolution Theorem, the Fourier Transform of the image is equal to the Fourier Transform of the object multiplied by the Optical Transfer Function (OTF):

$$i(\mathbf{x}) = o(\mathbf{x}) \otimes h(\mathbf{x})$$

$$\mathcal{F}\{i(\mathbf{x})\} = \mathcal{F}\{o(\mathbf{x})\} \times \mathcal{F}\{h(\mathbf{x})\}. \tag{2.11}$$

In this equation, $\otimes$ is the convolution operation. Typically, the only information known is the blurred image and an imperfect point spread function–this is known as *blind deconvolution* [19]. By using multiple frames with their respective measured point spread functions the number of solutions to the blind deconvolution can be reduced [35]. This is known as *multiframe* blind deconvolution and is an important technique used for image

11

restoration [5][35].

In 1970, Antoine Labeyrie observed that the *speckles* in a short exposure image contained more spatial frequency data when compared to a long exposure image [20]. The processes that use this speckle information to reconstruct an image is referred to as *speckle imaging*. There are two main steps to speckle imaging. First, to estimate the object and reference star intensity and second, to recover the phase that is lost from the first step [3]. Step one will be described in this section and two methods of phase recovery will be covered in the next two subsections.

Speckle interferometry is a technique used to find the expected value of the modulus of the Fourier Transform of the object. If the source object happens to be two points the cosine *fringe* patterns can be seen (see Figure 2.2).

If α_s represents the angular separation of a binary pair and, $\frac{\lambda}{D} \leq \alpha_s \leq \frac{\lambda}{r_0}$, where $\frac{\lambda}{D}$ is the approximate smallest angular separation two points are detectable in a diffraction limited environment and $\frac{\lambda}{r_0}$ is the smallest approximate angular separation two points can be detected through atmospheric turbulence then speckle interferometry can be useful [31], where r_0 is the Fried's seeing parameter and λ is the wavelength of light. If $\alpha_s < \frac{\lambda}{D}$, then the angular separation is too small to resolve. If $\alpha_s > \frac{\lambda}{r_0}$, then speckle interferometry will not improve the resolution. It is therefore assumed going forward that the binary separation angle, α_s, falls within the range above, where deconvolution is helpful.

First consider the irradiance incident on a detector. If the imaging system is properly focused on the object, we have the incident irradiance equal to the object irradiance as observed from geometry alone convolved with the PSF:

$$d(\mathbf{x}) = \sum_{\mathbf{y}} h(\mathbf{x} - \mathbf{y})o(\mathbf{y}) \tag{2.12}$$

where $d(\mathbf{x})$ is a single measured short exposure image, $h(\mathbf{y})$ is the PSF, and $o(\mathbf{y})$ is the diffraction-limited object irradiance. If the source object is a binary, let $o(\mathbf{y}) =$

12

$o_1\delta(\mathbf{y}) + o_2\delta(\mathbf{y} - \mathbf{y}_1)$, where δ is the Dirac function and o_1 and o_2 are the intensities of the binary points. Taking the convolution and applying the sifting property of integrating a Dirac function yields:

$$d(\mathbf{x}) = \sum_{\mathbf{y}} o_1 h(\mathbf{x} - \mathbf{y})\delta(\mathbf{y}) + \sum_{\mathbf{y}} o_2 h(\mathbf{x} - \mathbf{y})\delta(\mathbf{y} - \mathbf{y}_1)$$

$$= o_1 h(\mathbf{x}) + o_2 h(\mathbf{x} - \mathbf{y}_1).$$

(2.13)

Now take the Fourier transform of $d(\mathbf{x})$:

$$\mathcal{F}\{d(\mathbf{x})\} = o_1\mathcal{H}(\mathbf{f}) + o_2\mathcal{H}(\mathbf{f})e^{-j2\pi\mathbf{y}_1 f_x}.$$

(2.14)

Here we take the modulus squared of the result:

$$|\mathcal{F}\{d(\mathbf{x})\}|^2 = \left(O_1\mathcal{H}(\mathbf{f}) + O_2\mathcal{H}(\mathbf{f})e^{-j2\pi\mathbf{y}_1 f_x}\right) \times \left(O_1\mathcal{H}(\mathbf{f})^* + O_2\mathcal{H}(\mathbf{f})^* e^{j2\pi\mathbf{y}_1 f_x}\right)$$

$$= O_1^2|\mathcal{H}(\mathbf{f})|^2 + O_2^2|\mathcal{H}(\mathbf{f})|^2 + 2 \times REAL\left\{O_1 O_2|\mathcal{H}(\mathbf{f})|^2 e^{-j2\pi\mathbf{y}_1 f_x}\right\}$$

(2.15)

noting that $REAL\left\{e^{-j2\pi\mathbf{y}_1 f_x}\right\} = \cos(2\pi\mathbf{y}_1 f_x)$ reducing Equation 2.15 to:

$$|\mathcal{F}\{d(\mathbf{x})\}|^2 = O_1^2|\mathcal{H}(\mathbf{f})|^2 + O_2^2|\mathcal{H}(\mathbf{f})|^2 + 2O_1 O_2|\mathcal{H}(\mathbf{f})|^2 \cos(2\pi\mathbf{y}_1 f_x)$$

(2.16)

divide both sides by $|\mathcal{H}(\mathbf{f})|^2$, yields:

$$\frac{|\mathcal{F}\{d(\mathbf{x})\}|^2}{|\mathcal{H}(\mathbf{f})|^2} = O_1^2 + O_2^2 + 2O_1 O_2 \cos(2\pi\mathbf{y}_1 f_x).$$

(2.17)

Let $Q(\mathbf{f}) = |\mathcal{F}\{d(\mathbf{x})\}|^2 - K$, where K is the photon noise bias governed by Poisson statistics and $Q(\mathbf{f})$ is the unbiased speckle interferometry estimator [13]. The signal-to-noise ratio, SNR_Q, of $Q(\mathbf{f})$ improves as follows:

$$SNR_Q^N(\mathbf{f}) = \sqrt{N} \times SNR_Q(\mathbf{f})$$

(2.18)

where SNR_Q^N is the signal-to-noise ratio of N averaged independent realizations of $Q(\mathbf{f})$ [31]. Values of N, the number of short exposure images, range from a few hundred to

13

several thousand [31]. Assuming $N > 1$, it is necessary to take the expected value of both the numerator and denominator of Equation 2.17:

$$\frac{E\{|\mathcal{F}\{i(\mathbf{x})\}|^2\}}{E\{|\mathcal{H}(\mathbf{f})|^2\}} = O_1^2 + O_2^2 + 2O_1O_2 \cos(2\pi\mathbf{y}_1 f_x) \qquad (2.19)$$

where $i(\mathbf{x})$ is the detection plane irradiance of N images, $\mathcal{H}(\mathbf{f})$ is the OTF and $\mathbf{y}_1$ is the separation of the binary stars, $O_1(\mathbf{f})$ and $O_2(\mathbf{f})$ is the image spectrum of the binary stars. Plotting the results of Equation 2.19 can reveal a cosine pattern if the angular separation of the binary pair is large enough [14][20][31].

The following is a simulated example of speckle interferometry using 200 independent images of two point sources.
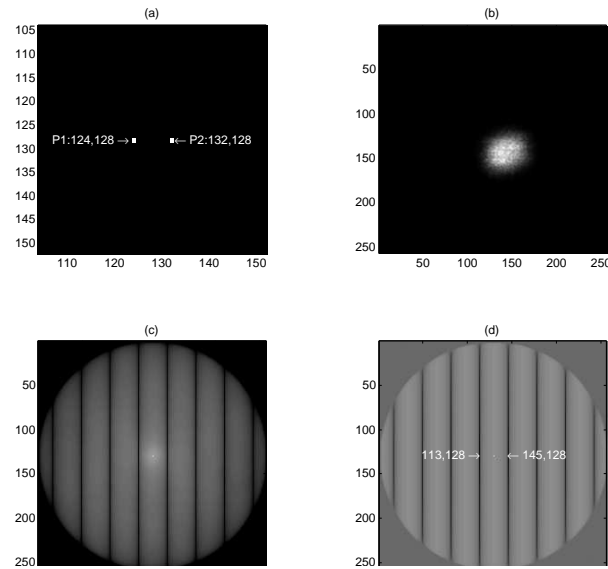
Figure 2.2: Speckle interferometry simulation with 200 independent frames. (a) The binary source image, (b) the simulated average of short exposure images, (c) speckle transfer function, (d) speckle transfer function showing fringe spacing.

In Figure 2.2 (a) the binary source image is shown, note the separation is 8 pixels; (b) is the simulated average of 200 short exposure images; (c) is the calculated unbiased speckle

14

interferometry estimator, $Q(\mathbf{f})$ (log scale); finally, (d) shows the log scale of $\frac{Q(\mathbf{f})}{E\{|\mathcal{H}(\mathbf{f})|^2\}}$. The binary separation from the original image, $\mathbf{y}_1$ can be calculated from the results. First looking at Equation 2.19, the period of the fringe pattern detected depends on $cos(2\pi\mathbf{y}_1 f_x)$. Where $\mathbf{y}_1$ is a 2-tuple and denotes the location of the second binary point in the image plane and f_x is the size of a pixel in the frequency plane. The peak-to-peak period in pixel count of the cosine fringes in Figure 2.2 (d) is 32:

$$P = Period = \frac{1}{frequency} = \frac{1}{\mathbf{y}_1 \Delta f_x}$$
$$\Delta f_x = \frac{1}{N}$$

(2.20)

where $N = 256$, the number of pixels and Δf_x is the sample size in the frequency plane.

$$P = Period = \frac{256}{\mathbf{y}_1}$$

from measurements, P=32 pixels :

$$32 = \frac{256}{\mathbf{y}_1}$$
$$\mathbf{y}_1 = \frac{256}{32} = 8 \text{ pixels.}$$

(2.21)

Looking at the simulation parameters, 8 pixels was the binary separation used to generate the image. The actual physical interpretation of 8 pixels of separation will depend on the characteristics of the imaging system and distance to the object being viewed. Thus, by measuring the pixel separation of the binary fringe pattern an estimation can be made as to the actual binary separation in the object plane.

Observing these cosine fringe patterns is a proven method of finding binary point sources. However, as mentioned before, the phase data is lost after taking the second moment of the image spectrum. This phase data needs to be recovered for image reconstruction. The next two subsections will discuss two common methods of phase retrieval.

15

2.1.2.1 Knox-Thompson.

As stated before, to properly reconstruct an image using spectral imaging the phase of the source object needs to be recovered. The first technique commonly used is the Knox-Thompson or cross spectrum method. Dr. K. T. Knox and B. J. Thompson published a paper in the Astrophysics Journal in 1974 describing a method of recovering images from atmospherically-degraded short exposure images [18][31]. This method is now called the Knox-Thompson Technique or the cross spectrum technique. In their paper, they defined the cross spectrum, $C(\mathbf{f}, \Delta\mathbf{f})$, as:

$$C(\mathbf{f}, \Delta\mathbf{f}) = I(\mathbf{f})I^*(\mathbf{f} + \Delta\mathbf{f}) \tag{2.22}$$

where $I(\mathbf{f}) = O(\mathbf{f})H(\mathbf{f})$ and $O(\mathbf{f})$ is the object spectrum, and $H(\mathbf{f})$ is the OTF [31][18].

The cross spectrum of the detected image is not directly proportional to the cross spectrum of the object as a bias term needs to be accounted for to properly estimate the phase [2][4][31]. If we assume individual pixels in the detection plane are statistically independent and the photon arrival is governed by Poisson statistics, then the unbiased cross spectrum for a single measured image, $d(\mathbf{x})$, can be written as [31]:

$$C_u(\mathbf{f}, \Delta\mathbf{f}) = D(\mathbf{f})D^*(\mathbf{f} + \Delta\mathbf{f}) - D^*(\Delta\mathbf{f}). \tag{2.23}$$

The term $D^*(\Delta\mathbf{f})$ is the conjugate of the image spectrum at $\Delta\mathbf{f}$, and is defined by:

$$D^*(\Delta\mathbf{f}) = \sum_{\mathbf{x}} d(\mathbf{x})e^{-j2\pi\Delta\mathbf{f}\cdot\mathbf{x}} \tag{2.24}$$

which will be different from image to image and needs to be subtracted out before taking the average of the short exposure images. Each image also needs to be centered as the cross spectrum method is not shift invariant [2][4][18][31].

Typical values of $\Delta\mathbf{f} = (\Delta f_1, \Delta f_2)$, the spatial frequency offset, are, $|\Delta\mathbf{f}| < r_0/(\lambda d)$, where r_0 is the Fried seeing parameter, λ is the wavelength of the light and d is the distance

from the pupil plane to the imaging plane [2][31]. Taking the average cross spectrum over multiple short exposure images yields the following equation [2][31]:

$$E[C(\mathbf{f}, \Delta\mathbf{f})] = |O(\mathbf{f})||O(\mathbf{f} + \Delta\mathbf{f})|e^{j[\phi_o(\mathbf{f}) - \phi_o(\mathbf{f} + \Delta\mathbf{f})]}E[H(\mathbf{f})H^*(\mathbf{f} + \Delta\mathbf{f})] \qquad (2.25)$$

where second moment of the OTF, $E[H(\mathbf{f})H^*(\mathbf{f}+\Delta\mathbf{f})]$, is the *cross spectrum transfer function* and relates the object spectrum, $O(\mathbf{f})$ to the cross spectrum. The cross spectrum transfer function is real-valued, so the phase of the average cross spectrum is [2][4][31]:

$$\phi_C(\mathbf{f}, \Delta\mathbf{f}) = \phi_o(\mathbf{f}) - \phi_o(\mathbf{f} + \Delta\mathbf{f}). \qquad (2.26)$$

The object phase, ϕ_o can be extracted from this equation. Let the offset vector in the x direction be Δf_x and the offset vector in the y direction be Δf_y, that is $\Delta\mathbf{f} = (\Delta f_x, \Delta f_y)$. The phase differences generated by these offset vectors are [2][31]:

$$\Delta\phi_x(f_x, f_y) = \phi_o(f_x, f_y) - \phi_o(f_x + \Delta f_x, f_y) \qquad (2.27)$$

$$\approx \frac{\partial\phi_o(\mathbf{f})}{\partial f_x}\Delta f_x \qquad (2.28)$$

$$\Delta\phi_y(f_x, f_y) = \phi_o(f_x, f_y) - \phi_o(f_x, f_y + \Delta f_y) \qquad (2.29)$$

$$\approx \frac{\partial\phi_o(\mathbf{f})}{\partial f_y}\Delta f_y \qquad (2.30)$$

The partial derivatives form the orthogonal components of the gradient of the object phase spectrum, $\nabla\phi_o(\mathbf{f})$. This angle data can be combined with the magnitude data retrieved from speckle interferometry methods to reconstruct the image [2][31]. Calculating $\phi_o(\mathbf{f})$ can be accomplished by the following equation:

$$\phi_o(N_x\Delta f_x, N_y\Delta f_y) = \sum_{i=0}^{N_x-1}\Delta\phi_x(i\Delta f_x, 0) + \sum_{j=0}^{N_y-1}\Delta\phi_y(0, j\Delta f_y) \qquad (2.31)$$

where N_x and N_y are the number of pixels in the x and y direction in the image plane. For the simulations in this paper, $\Delta f_x = \Delta f_y = 1$, which provides a small offset constant without doing sub-pixel manipulations. Looking at Equation 2.31, each point in the reconstructed

17

object phase, ϕ_o, can be obtained by taking the angle of the average cross spectrum in both x and y directions and then summing along the x and y axis to the desired phase coordinate to reconstruct [31]. Many summing paths can be taken to get to a particular phase coordinate. In a noise free environment all paths to a particular point will yield the same result. In a real-world system, each path will yield slightly different results depending on random noise effects. It is, therefore, a standard practice to calculate the object phase at a particular point by averaging the results of summing several paths to that point [2][31].

The result of implementing Equation 2.31 is an unwrapped phase 2D-matrix containing the reconstructed object phase in the Fourier domain. To get the reconstructed image, ϕ_o needs to be wrapped and then multiplied by the Fourier transform of the intensity information obtained through, in this case, speckle interferometry. The following is a simulated example of a basic implementation of the Knox-Thompson or cross spectrum method. The reconstructed image is formed from the following equation:

$$o(x, y) = |\mathcal{F}^{-1}\{|O|e^{-j\phi_o}\}| \tag{2.32}$$

where O is the modulus of the average object intensities calculated using speckle interferometry and ϕ_o is the object phase recovered by the cross spectrum method and $o(x, y)$ is the reconstructed object.

Figure 2.3 shows the sum of 50 short exposure images of a binary point source with a separation of 4 pixels on a 255 pixel square grid. Each image passed through a randomly generated phase screen with an r_o value of 30 cm to simulate atmospheric blur. Poisson noise was added to the data calculated at the image plane. A focused telescope with a square aperture of 1 meter was used for this simulation. Figure 2.4 is the result of my implementation of the cross spectrum method described in this section when applied to the image data from Figure 2.3.
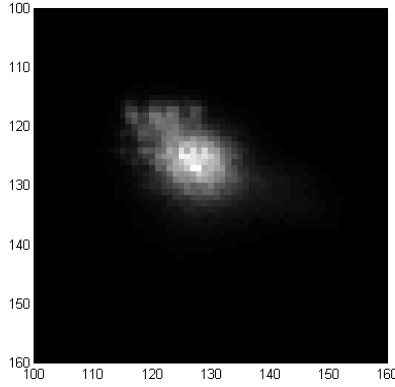
Figure 2.3: Stack of 50 short exposure images, each simulated through a unique random phase screen with $r_o = 30$ cm.

Implementing a robust cross spectrum phase retrieval algorithm requires extensive fine tuning to remove as much noise as possible. Please refer to Ayers work for more information on implementation [2].

Reconstructing a higher resolution image is typically what is desired in astronomical imaging. A major difference between the multi-hypothesis method and phase reconstruction is the focus on detecting binaries versus producing higher resolution images. One other phase reconstruction method should be mentioned and that is bispectrum technique.

2.1.2.2 Bispectrum.

The bispectrum is another effective method used to reconstruct the phase of an image. It is invariant to image shift, which is a valuable property when looking at multiple images of potential binaries [2][22]. It is defined as [31]:

$$B(\mathbf{f}_1, \mathbf{f}_2) = D(\mathbf{f}_1)D(\mathbf{f}_2)D^*(\mathbf{f}_1 + \mathbf{f}_2). \tag{2.33}$$

Note the phase of the object spectrum is contained in the phase of the bispectrum at three points in frequency space ($\mathbf{f}_1$, $\mathbf{f}_2$, and $\mathbf{f}_1 + \mathbf{f}_2$) compared to the cross spectrum which needs two points to reconstruct the object phase. Many different techniques have been and

19
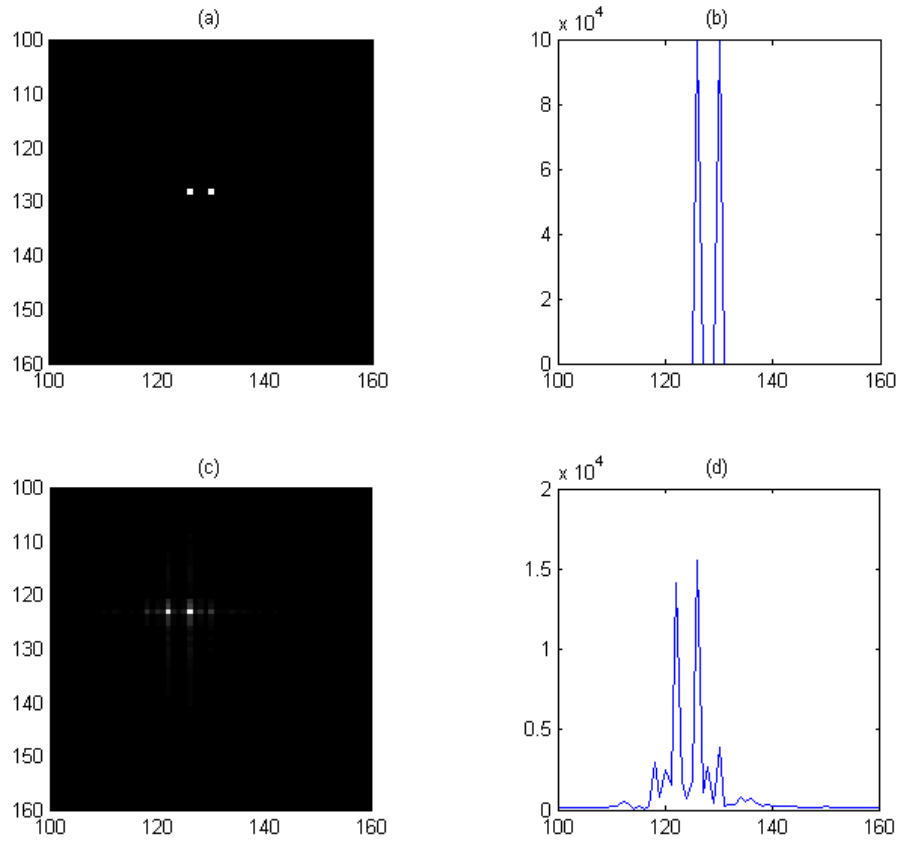
Figure 2.4: Result of cross spectrum method with $r_o = 30cm$, original image (a), cross section of original image (b), reconstructed image (c), cross section of reconstructed image (d).

are continued to be published on how best to calculate the phase using the bispectrum [2][21][24][25][26]. I will highlight one such method which is the unit amplitude phasor recursive reconstructor.

To begin, the unbiased bispectrum for a single short exposure image is:

$$B_u(\mathbf{f}_1, \mathbf{f}_2,) = D(\mathbf{f}_1)D(\mathbf{f}_2)D^*(\mathbf{f}_1 + \mathbf{f}_2) - |D(\mathbf{f}_1)|^2 - |D(\mathbf{f}_2)|^2 - |D(\mathbf{f}_1 + \mathbf{f}_2)|^2 - 2K + 3P\sigma_n^2 \quad (2.34)$$

where K is the bias caused by the random arrival of photons governed by Poisson statistics and $P\sigma_n^2$ represents additive noise caused by the imaging device [31]. The unbiased bispectrum is calculated for each short exposure image and then the average bispectrum is computed. The phase of the resulting mean bispectrum is:

$$\phi_B(\mathbf{f}_1, \mathbf{f}_2) \tag{2.35}$$

which is equal to [2][22][31]:

$$\phi_B(\mathbf{f}_1, \mathbf{f}_2) = \phi_O(\mathbf{f}_1) + \phi_O(\mathbf{f}_2) - \phi_O(\mathbf{f}_1 + \mathbf{f}_2). \tag{2.36}$$

Given we have calculated the bispectrum phase, $\phi_B(\mathbf{f}_1, \mathbf{f}_2)$, we need to know two other values of the object phase spectrum to then iteratively calculate all other remaining values for the object phase. A typical approach is to set:

$$\phi_O(0,0) = \phi_O(1,0) = \phi_O(-1,0) = \phi_O(0,1) = \phi_O(0,-1) = 0. \tag{2.37}$$

Thus:

$$\phi_O((0,0) + (0,0)) = -\phi_B((0,0),(0,0))$$

$$\phi_O((1,0) + (0,0)) = -\phi_B((1,0),(0,0))$$

$$\phi_O((-1,0) + (0,0)) = -\phi_B((-1,0),(0,0)) \tag{2.38}$$

$$\phi_O((0,0) + (0,1)) = -\phi_B((0,0),(0,1))$$

$$\phi_O((0,0) + (0,-1)) = -\phi_B((0,0),(0,-1)).$$

Much like the cross spectrum, many different combinations of known values can be used to find a value at an unknown location. For example, if the point object phase spectrum $\phi_O(4,5)$ is desired, then:

$$\phi_O(4,5) = \phi_O(1,0) + \phi_O(3,5) - \phi_B((1,0),(3,5))$$

$$= \phi_O(1,0) + \phi_O(3,5) - \phi_B((1,0),(3,5))$$

$$= \phi_O(2,3) + \phi_O(2,2) - \phi_B((2,3),(2,2)) \tag{2.39}$$

$$= \phi_O(3,4) + \phi_O(1,1) - \phi_B((3,4),(1,1))$$

21

and so forth. Each linear combination does not necessarily give the same results if noise is present. Thus, like the cross spectrum method, many paths are typically calculated and then averaged [21][31]. Lastly, due to a potential 2π bias when taking different paths, the calculations are typically done as unit phasors, thus, the final algorithm for reconstructing phase using the bispectrum is [21]:

$$e^{j\phi_O(\mathbf{f}_1+\mathbf{f}_2)} = e^{j\phi_O(\mathbf{f}_1)}e^{j\phi_O(\mathbf{f}_2)}e^{j\phi_B(\mathbf{f}_1,\mathbf{f}_2)}. \tag{2.40}$$

No example of implementing the bispectrum method is provided in this paper. The reader can refer to the following references for examples and more information, [2][21][24][25][26].

Both the cross spectrum and bispectrum method have proven to be effective at reconstructing atmospherically blurred images to reveal binary pairs. However, as has been discussed before, if the object is *only* binary detection, then complete image reconstruction is unnecessary. By comparing the statistics of two hypothetical sources, i.e., a single and binary, better results for binary detection can be had then by visually inspecting reconstructed images. The next section will discuss another method of image reconstruction useful in binary detection, imaging by correlation.

2.1.3 *Imaging by Correlation.*

This method of image recovery utilizes a process developed to recover meaningful information from random data and applies it to the problem of image recovery from second and third order correlation. This technique is unique in the fact that it simultaneously recovers the Fourier magnitude and phase as compared with speckle imaging in which amplitude and phase are recovered separately [34].

In general, correlation is an Nth order process so thus for the purposes of binary detection $N = 2$, referred to as autocorrelation, will be used. The general strategy is to take the autocorrelation of the measured image data and the autocorrelation of an estimated image and then iterate through a log likelihood cost function to reduce the estimated image

to the most likely true image [34].

Let $R(\mathbf{y})$ be the autocorrelation function of the measured image data, $d(\mathbf{x})$, where $R(\mathbf{y}) = \sum_{\mathbf{x}=1}^{N} d(\mathbf{x})d(\mathbf{x}+\mathbf{y})$, the summation representing the sum over all pixels in d. Let $R_\lambda(\mathbf{y})$ be the autocorrelation of the estimated image, $\lambda(\mathbf{x})$. Any cost function can be used, however in this work the I-divergence $D(R_\lambda, R)$ function used by Schulz and Snyder is adopted [34]:

$$D(R, R_\lambda) = \sum_{\mathbf{y}} [R_\lambda(\mathbf{y}) - R(\mathbf{y})] + \sum_{\mathbf{y}} R(\mathbf{y}) ln \frac{R(\mathbf{y})}{R_\lambda(\mathbf{y})}. \tag{2.41}$$

By minimizing the I-divergence cost function we can solve for a $\lambda(\mathbf{x})$ that is the most likely true image. Taking the derivative of $D(R_\lambda, R)$ with respect to a single point in the estimated image and then setting that equal to zero yields the necessary optimality condition:

$$\frac{\partial D(R_\lambda, R)}{\partial \lambda(\mathbf{x}_o)} = \sum_{\mathbf{y}} [\lambda(\mathbf{x}_o + \mathbf{y}) + \lambda(\mathbf{x}_o - \mathbf{y})] - \sum_{\mathbf{y}} \frac{R(\mathbf{y})}{R_\lambda(\mathbf{y})} [\lambda(\mathbf{x}_o + \mathbf{y}) + \lambda(\mathbf{x}_o - \mathbf{y})] = 0. \tag{2.42}$$

Schulz and Snyder then setup an algorithm that iteratively solves for an updated $\lambda(\mathbf{x})$ based on a previous one [34]. For k iterations:

$$\lambda_{k+1}(\mathbf{x}) = \lambda_k(\mathbf{x}) \frac{1}{R_o^{1/2}} \sum_{\mathbf{y}} \lambda_k(\mathbf{x}+\mathbf{y}) \frac{[R(\mathbf{y}) + R(-\mathbf{y})]}{2R_{\lambda k}(\mathbf{y})} \tag{2.43}$$

where R_o is the autocorrelation evaluated at $y = 0$ of the measured data. Using the convolution and correlation theorems, multiplication can be used in the Fourier domain. For k iterations, an estimated reconstructed image, $\lambda_k(\mathbf{x})$ is found [34]. The autocorrelation is similar to the bispectrum in that image tilt does not need to be removed before processing.

Figure 2.5 shows a simulated result after 100 iterations. Figure 2.6 shows the simulated result compared to the original image. The same simulation parameters used in the cross spectrum example in Section 2.1.2.1 were used. The software implementation of this method is discussed more in Chapter 3, as it is used as a comparison to the multi-hypothesis technique proposed in this paper.
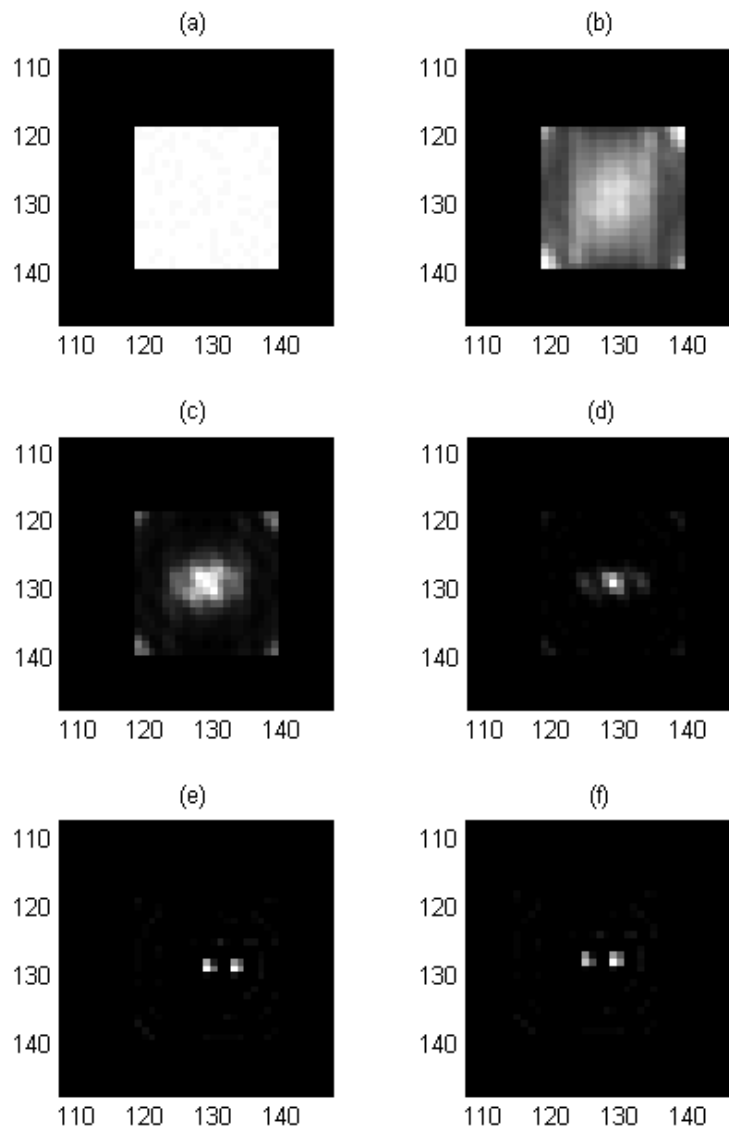
Figure 2.5: Results with different numbers of iterations: (a) 1, (b) 5, (c) 10, (d) 15, (e) 80, and (f) 100 iterations.
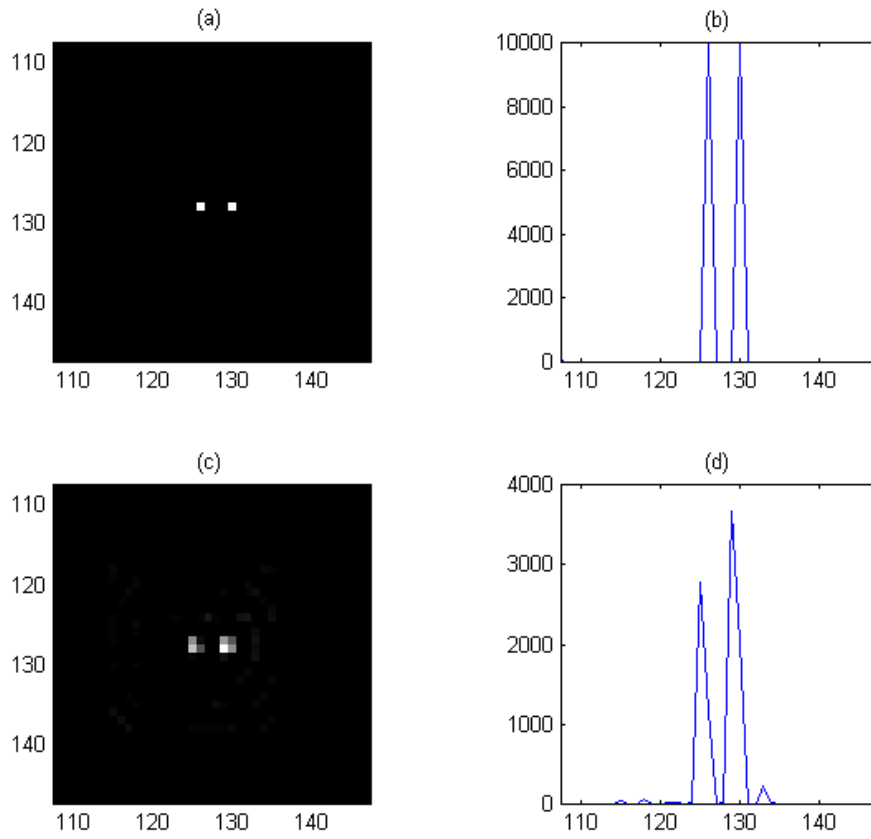
Figure 2.6: Results of the correlation technique: (a) original image, (b) original image cross section, (c) reconstructed image, and (d) reconstructed image cross section.

2.1.4   Binary detection by post-process image reconstruction summary.

Image reconstruction via cross correlation, bispectrum and autocorrelation are all proven techniques that can enhance image spatial resolution and thus greatly impact binary detection.   This section provided information for a basic understanding of how these methods can enhance images.

This thesis will compare one of the methods listed above, image reconstruction by autocorrelation, to a statistical approach that does not provide a reconstructed image but focuses on the question–*Was this image created by a single or binary point source(s)*? The next section will provide an overview of how a multi-hypothesis technique can be setup to answer this question.

2.2   Multi-Hypothesis Detection

By assuming a source signal is either a zero, one, et cetera and calculating the expected value of each hypothesis, the most likely original signal can be determined.   This very simple yet powerful logic is foundational to digital communication and other areas of electo optics such as Light Detection And Ranging (LiDAR) [29]. The same logic can be used in detecting binaries that have been distorted by the atmosphere.

If we can measure how the atmosphere distorts a point source and simulate how that same atmosphere would distort various combinations of binary sources we can predict what an image should look like if it was the result of a binary or single point source, as perceived from the pupil plane of an imaging system. We can then compare what the image should look like given a single or binary point source to what was actually imaged through that same atmosphere. In this way a binary can be detected based on what we expect to see given two different scenarios, or hypothesis.

Figure 2.7 shows the basic concept behind this idea.   One of the most important assumptions made for using this technique is that a valid point spread function (PSF) can be measured that correlates to the image being analyzed for a potential binary. Another

important assumption, and an area for future research, is to assume more than just two scenarios to detect larger clusters then just a binary. Hypothesis for three, four, and so forth, as well as different shapes can all be used as comparisons for the image that was actually detected. The derivation of and detailed analysis of a proposed multi-hypothesis algorithm to detect binaries is given in Chapter 3. Results of simulated and measured data testing will be given in Chapter 4.

Multi-Hypothesis for Binary Detection Overview

1 Measure Data

Measured Image

Measured PSF

2 Calculate Log-likelihoods

Hypothesis Zero

Determine if image intensity is below minimum threshold for detection.

Hypothesis One

Calculate most likely intensity and position of single point source to produce measured image

Hypothesis Two

Calculate most likely intensity and position of two point sources to produce measured image

3 Binary Decision

Based on detection criteria determine which hypothesis is most likely

Figure 2.7: Overview of binary hypothesis method. Chapter 3 will work through derivations of each step.

2.3   Chapter Summary

As binary objects become closer and dimmer, detection becomes impossible for a standard imaging system. Using adaptive optics, looking for patterns, extracting higher resolution from speckle images, and estimating the image using correlation are current methods for binary detection. This thesis will explore a method that has not been used in astronomy for binary detection, referred to herein as the multi-hypothesis technique. Basically, by measuring the PSF we can calculate what a single point source and a binary source would look like, then compare that to what is detected. The result of this comparison can be used to make a statistical determination on whether the image detected was the result of a single point source or a binary point source.

III.   Methodology

THIS chapter will walk through the derivation and implementation of the multi-hypothesis algorithms that are investigated in this thesis. The goal is to provide the reader with a guide to repeat the results and conclusions contained in Chapters 4 and 5. Computer simulations and processing were conducted using Matlab™. It is important to note that from this point forward all simulations will be single-frame short-exposure images where the PSF is perfectly known.

The following table is provided as a quick reference of the different variables, operations, and units used in this chapter.

Table 3.1: Common symbols.

Symbol	Meaning
$\mathbf{x}$	rectangular coordinate vector in the true image plane
$\mathbf{y}$	rectangular coordinate vector in the detection plane
$d(\mathbf{y})$	single, short exposure image
$\lambda(\mathbf{x})$	true image
$h(\mathbf{y})$	Point Spread Function, PSF
δ	Dirac function
E	expectation operator
$\mathcal{F}$	Fourier Transform
N^2	Number of pixels in the image

3.1 Derivation of multi-hypothesis algorithms

Given an atmospherically blurred image and a PSF corresponding to that image, the question of weather that image contains a binary, single object or nothing can be determined using a hypothesis-based model. This thesis will compare the results of three hypothesis. First, that the source or true image does not contain any points. Second, that the image was formed by a single point source. The third hypothesis is that the image was formed by two point sources. It will be shown that the proposed algorithm can quickly determine which hypothesis is the most likely. Thresholds to control false alarm rates can be incorporated into the process to ensure a very high confidence of correctly detecting a binary. Obtaining a valid PSF is not trivial but is not the topic of this thesis. Instead, the assumption is made that a valid PSF can be obtained via wavefront sensor measurements. The next three subsections will walk through the derivation of the zero, single and double point source hypothesis algorithms.

3.1.1 Zero point source derivation.

The first hypothesis, referred to herein as hypothesis zero, is derived by assuming the true image, $\lambda(\mathbf{x})$, contains only background noise. Let b_n be the median background noise of the detected image, $d(\mathbf{y})$. The expected value of the detected image can be written as the discrete convolution of the true image with the PSF, $h(\mathbf{y})$ [14]:

$$
\begin{aligned}
E[d(\mathbf{y})] &= \sum_{\mathbf{x}=1}^{N} \lambda(\mathbf{x}) h(\mathbf{y} - \mathbf{x}) \\
&= \sum_{\mathbf{x}=1}^{N} b_n h(\mathbf{y} - \mathbf{x}).
\end{aligned}
\tag{3.1}
$$

By definition of the OTF, $h(\mathbf{y})$, the sum over all points is equal to unity regardless of how it is shifted, giving:

$$
E[d(\mathbf{y})] = b_n.
\tag{3.2}
$$

If we now make the assumption that each pixel in the detected image is statistically independent and note that photon arrival is governed by Poisson statistics [13][14], the

30

joint probability mass function for hypothesis zero can be written as:

$$\prod_{y=1}^{N} P[d(\mathbf{y})] = \prod_{y=1}^{N} \left[\frac{(b_n)^{d(\mathbf{y})} e^{-b_n}}{d(\mathbf{y})!} \right].$$ (3.3)

By taking the natural log of Equation 3.3 we can calculate a value of the log-likelihood that can be used to compare to hypothesis one and two. Let LL_{h0} be the log-likelihood of hypothesis zero:

$$\begin{aligned}
LL_{h0} &= \ln \left[\prod_{y=1}^{N} P[d(\mathbf{y})] \right] \\
&= \ln \left[\prod_{y=1}^{N} \left[\frac{[b_n]^{d(\mathbf{y})} e^{-b_n}}{d(\mathbf{y})!} \right] \right] \\
&= \sum_{y=1}^{N} \left[\ln \left[[b_n]^{d(\mathbf{y})} \right] + \ln \left[e^{-b_n} \right] - \ln[d(\mathbf{y})!] \right] \\
&= \sum_{y=1}^{N} \left[d(\mathbf{y}) \left(\ln[b_n] \right) - b_n - \ln[d(\mathbf{y})!] \right].
\end{aligned}$$ (3.4)

The final line of Equation 3.4 can be used to test against the log-likelihood values of the other hypothesis equations to determine if an image contains zero, one or two point sources. A simpler method can be used however by simply setting a threshold based on a tolerance for false detection. Any image with a median photon count below this threshold can be removed from further processing. Later in this chapter a method for calculating this threshold will be given.

3.1.2   *Single point source derivation.*

The next hypothesis assumes a single point source and is referred to as hypothesis one in this paper. If the true image, $\lambda(\mathbf{x})$, is assumed to contain a single point source with amplitude α_0, it can be written as:

$$\lambda(\mathbf{x}) = \alpha_0 \delta(\mathbf{x} - \mathbf{x}_0).$$ (3.5)

Equation 3.5 does not account for background noise. There are several methods used to calculate the background noise in an image. Taking the median of the photon count of

what is considered to be *empty space* surrounding the object of interest is one way to estimate a single photon value for background noise at each pixel location. Using this approximation, the hypothesized true image can be represented by the following equation, where b_n represents the median background noise of the detected image:

$$\lambda(\mathbf{x}) = \alpha_0 \delta(\mathbf{x} - \mathbf{x}_0) + b_n. \tag{3.6}$$

Let $d(\mathbf{x})$ be a single detected image. The expected value of the detected image at pixel location $\mathbf{y}$, $d(\mathbf{y})$, can be written as the discrete convolution of the true image $\lambda(\mathbf{x})$ with the transfer function, $h(\mathbf{y})$ [14]:

$$E[d(\mathbf{y})] = \sum_{\mathbf{x}=1}^{N} \lambda(\mathbf{x}) h(\mathbf{y} - \mathbf{x}) \tag{3.7}$$

Substituting Equation 3.6 into 3.7 gives:

$$E[d(\mathbf{y})] = \sum_{\mathbf{x}=1}^{N} \left(\alpha_0 \delta(\mathbf{x} - \mathbf{x}_0) + b_n \right) h(\mathbf{y} - \mathbf{x}) \tag{3.8}$$

and applying the sifting property of a Dirac and distributing the transfer function yields:

$$E[d(\mathbf{y})] = \alpha_0 h(\mathbf{y} - \mathbf{x}_0) + \sum_{\mathbf{x}=1}^{N} b_n h(\mathbf{y} - \mathbf{x}). \tag{3.9}$$

By definition, the sum of the normalized transfer function, in this case $h(\mathbf{y})$, over all pixels is equal to one, so Equation 3.9 reduces to:

$$E[d(\mathbf{y})] = \alpha_0 h(\mathbf{y} - \mathbf{x}_0) + b_n. \tag{3.10}$$

The arrival of detected photons is assumed to be governed by Poisson statistics [13]. Furthermore, we assume each pixel in the detection plane is statistically independent. These two assumptions allow us to write the joint Probability Mass Function (PMF) of the detected image as:

$$\prod_{\mathbf{y}=1}^{N} P[d(\mathbf{y})] = \prod_{\mathbf{y}=1}^{N} \left[\frac{[\alpha_0 h(\mathbf{y} - \mathbf{x}_0) + b_n]^{d(\mathbf{y})} e^{-\alpha_0 h(\mathbf{y} - \mathbf{x}_0) - b_n}}{d(\mathbf{y})!} \right]. \tag{3.11}$$

32

To put Equation 3.11 in log-likelihood format we simply take the natural log of both sides. Let, LL_{h1} be the log-likelihood of hypothesis one such that:

$$
\begin{aligned}
LL_{h1} &= \ln\left[\prod_{\mathbf{y}=1}^{N} P[d(\mathbf{y})]\right] \\
&= \ln\left[\prod_{\mathbf{y}=1}^{N}\left[\frac{[\alpha_0 h(\mathbf{y}-\mathbf{x}_0)+b_n]^{d(\mathbf{y})} e^{-\alpha_0 h(\mathbf{y}-\mathbf{x}_0)-b_n}}{d(\mathbf{y})!}\right]\right] \\
&= \sum_{\mathbf{y}=1}^{N}\left[\ln\left[[\alpha_0 h(\mathbf{y}-\mathbf{x}_0)+b_n]^{d(\mathbf{y})}\right] + \ln\left[e^{-\alpha_0 h(\mathbf{y}-\mathbf{x}_0)-b_n}\right] - \ln[d(\mathbf{y})!]\right] \\
&= \sum_{\mathbf{y}=1}^{N}\left[d(\mathbf{y})\left(\ln[\alpha_0 h(\mathbf{y}-\mathbf{x}_0)+b_n]\right) - \alpha_0 h(\mathbf{y}-\mathbf{x}_0) - b_n - \ln[d(\mathbf{y})!]\right].
\end{aligned}
\tag{3.12}
$$

We want to maximize the function in the right hand side of Equation 3.12 so we need to find values for α_0 and $\mathbf{x}_0$ that provide the numerically greatest results. One effective method is to calculate a good estimate for α_0, substitute it into the log-likelihood in Equation 3.12 and then cycle through values for, $\mathbf{x}_0$ that maximizes LL_{h1}. The shift variable $\mathbf{x}_0$ that maximizes the log-likelihood is then used to find a more accurate value for α_0 using a Picard iteration technique that will be derived below. First, we need an approximation for the value of α_0. If we assume the true image is a single point source we can sum all photons in $d(\mathbf{y})$ and subtract the average background noise contained in each pixel to get an approximation for α_0. If there are N^2 pixels an initial guess for α_0 is:

$$
\alpha_0 = \sum_{\mathbf{y}=1}^{N}[d(\mathbf{y})] - N^2 b_n.
\tag{3.13}
$$

Substituting this choice of α_0 into the log-likelihood expression in Equation 3.12 we find a value for $\mathbf{x}_0$ that produces a maximum of LL_{h1}. The next step is to find a value for α_0 that maximizes the log-likelihood. To accomplish this we can take the partial derivative of the log-likelihood with respect to α_0 and set it equal to zero. Solving that equation and multiplying both sides by α_0 will put it in a form to apply the Picard iteration technique.

First, the partial derivative of the expression in Equation 3.12 with respect to α_0 is:

$$\frac{\partial}{\partial \alpha_0}\left(\ln\left[\prod_{\mathbf{y}=1}^{N} P[d(\mathbf{y})]\right]\right) = \frac{\partial}{\partial \alpha_0}\left(\sum_{\mathbf{y}=1}^{N} [d(\mathbf{y})(\ln[\alpha_0 h(\mathbf{y} - \mathbf{x}_0) + b_n]) - \alpha_0 h(\mathbf{y} - \mathbf{x}_0) - b_n - \ln[d(\mathbf{y})!]]\right)$$

$$0 = \sum_{\mathbf{y}=1}^{N}\left[\frac{d(\mathbf{y})h(\mathbf{y} - \mathbf{x}_0)}{\alpha_0 h(\mathbf{y} - \mathbf{x}_0) + b_n} - h(\mathbf{y} - \mathbf{x}_0) - 0 - 0]\right].$$

(3.14)

Again note that the sum over all pixels of the normalized PSF is unity, $\sum_{\mathbf{y}=1}^{N} h(\mathbf{y} - \mathbf{x}_0) = 1$, which reduces Equation 3.14 to:

$$1 = \sum_{\mathbf{y}=1}^{N}\left[\frac{d(\mathbf{y})h(\mathbf{y} - \mathbf{x}_0)}{\alpha_0 h(\mathbf{y} - \mathbf{x}_0) + b_n}\right].$$

(3.15)

If we multiply both sides of Equation 3.15 by α_0 we can create an iterative algorithm by applying the Picard technique. If we let n represent the iteration index, let the left side be the *new* α_0 such that our final update equation is:

$$\alpha_{0(n+1)} = \alpha_{0(n)}\sum_{\mathbf{y}=1}^{N}\left[\frac{d(\mathbf{y})h(\mathbf{y} - \mathbf{x}_0)}{\alpha_{0(n)}h(\mathbf{y} - \mathbf{x}_0) + b_n}\right].$$

(3.16)

The initial value for $\alpha_{0(n)}$ is the estimated value found in Equation 3.13. One method of determining how many iterations to run is to compare the variance between $\alpha_{0(n+1)}$ and $\alpha_{0(n)}$. Once the difference between the old and new alphas are within a desired value the iteration process can end. The final value of $\alpha_{0(n+1)}$ from Equation 3.16 along with the previously calculated value for $\mathbf{x}_0$ is entered a final time into the log-likelihood equation for hypothesis one, in Equation 3.12, to produce the number that will be compared with the other log-likelihood values from hypothesis zero and two.

The next section will derive the hypothesis two algorithms and follows the methodology in this section very closely.

3.1.3   Two point source derivation.

The final hypothesis we will look at, hypothesis two, assumes the true image, $\lambda(\mathbf{x})$, is two point sources with amplitude α_1 and α_2 with b_n again representing the average

background noise described in Section 3.1.2:

$$\lambda(\mathbf{x}) = \alpha_1 \delta(\mathbf{x} - \mathbf{x}_1) + \alpha_2 \delta(\mathbf{x} - \mathbf{x}_2) + b_n. \tag{3.17}$$

The expected value of the detected image at pixel location $\mathbf{y}$, $d(\mathbf{y})$, can be written as the discrete convolution of the true image $\lambda(\mathbf{x})$ with the transfer function, $h(\mathbf{y})$:

$$E[d(\mathbf{y})] = \sum_{\mathbf{x}=1}^{N} \lambda(\mathbf{x})h(\mathbf{y} - \mathbf{x}). \tag{3.18}$$

Similar to the hypothesis one, substituting the expression in Equation 3.17 into Equation 3.18 and applying the sifting property of a Dirac and noting once again that the sum of the optical transfer function over all pixels is unity, $\sum_{\mathbf{y}=1}^{N} h(\mathbf{y} - \mathbf{x}_0) = 1$, gives the following result:

$$E[d(\mathbf{y})] = \alpha_1 h(\mathbf{y} - \mathbf{x}_1) + \alpha_2 h(\mathbf{y} - \mathbf{x}_2) + b_n. \tag{3.19}$$

Photon arrivals in the detection plane are governed by Poisson statistics. Furthermore, we assume noise in each pixel in the detection plane is statistically independent. This allows us to write the joint PMF as:

$$\prod_{\mathbf{y}=1}^{N} P[d(\mathbf{y})] = \prod_{\mathbf{y}=1}^{N} \left[\frac{[\alpha_1 h(\mathbf{y} - \mathbf{x}_1) + \alpha_2 h(\mathbf{y} - \mathbf{x}_2) + b_n]^{d(\mathbf{y})} e^{-\alpha_1 h(\mathbf{y} - \mathbf{x}_1) - \alpha_2 h(\mathbf{y} - \mathbf{x}_2) - b_n}}{d(\mathbf{y})!} \right]. \tag{3.20}$$

As was done for hypothesis one, we will put Equation 3.20 into a log-likelihood format and simplify. Let LL_{h2} be the log-likelihood for hypothesis two which is equal to the natural

log of Equation 3.20:

$$
\begin{aligned}
LL_{h2} &= \ln\left[\prod_{\mathbf{y}=1}^{N} P[d(\mathbf{y})]\right] \\
&= \ln\left[\prod_{\mathbf{y}=1}^{N}\left[\frac{[\alpha_1 h(\mathbf{y}-\mathbf{x}_1)+\alpha_2 h(\mathbf{y}-\mathbf{x}_2)+b_n]^{d(\mathbf{y})} e^{-\alpha_1 h(\mathbf{y}-\mathbf{x}_1)-\alpha_2 h(\mathbf{y}-\mathbf{x}_2)-b_n}}{d(\mathbf{y})!}\right]\right] \\
&= \sum_{\mathbf{y}=1}^{N}\left[\frac{\ln\left[[\alpha_1 h(\mathbf{y}-\mathbf{x}_1)+\alpha_2 h(\mathbf{y}-\mathbf{x}_2)+b_n]^{d(\mathbf{y})}\right] + \ln\left[e^{-\alpha_1 h(\mathbf{y}-\mathbf{x}_1)-\alpha_2 h(\mathbf{y}-\mathbf{x}_2)-b_n}\right]}{\ln[d(\mathbf{y})!]}\right] \\
&= \sum_{\mathbf{y}=1}^{N}\left[\frac{d(\mathbf{y})\ln[\alpha_1 h(\mathbf{y}-\mathbf{x}_1)+\alpha_2 h(\mathbf{y}-\mathbf{x}_2)+b_n]-\alpha_1 h(\mathbf{y}-\mathbf{x}_1)-\alpha_2 h(\mathbf{y}-\mathbf{x}_2)-b_n}{\ln[d(\mathbf{y})!]}\right].
\end{aligned}
$$

(3.21)

The final result of Equation 3.21 is what will be implemented to calculate the log-likelihood of hypothesis two. There are four unknown variables needed to find the maximum value namely the most likely amplitude and pixel location of the hypothesized true image. As with hypothesis one, we can make a initial guess as to what the amplitude of α_1 and α_2 might be assuming the image, $d(\mathbf{y})$, contains two source points of light. In Section 3.1.2 we showed that a good estimate is to sum up the photons in the image, $d(\mathbf{y})$ and subtract off the estimated background noise photons. We can apply this same technique and simply assume that each point in the binary is equally as bright. During the iteration phase of this algorithm more accurate values for α_1 and α_2 will be descended on. So initial values can be written as:

$$
\alpha_1 = \alpha_2 = \frac{\sum_{\mathbf{y}=1}^{N}[d(\mathbf{y})] - N^2 b_n}{2}.
$$

(3.22)

Lastly we need to calculate an iterative algorithm for computing accurate values of α_1 and α_2. This can be accomplished using the same method applied to α_0, namely looking at the gradient with respect to α_1 and α_2. Starting with the partial derivative of Equation 3.21

with respect to α_1:

$$
\begin{aligned}
0 &= \frac{\partial}{\partial \alpha_1}(LL_{h2}) = \frac{\partial}{\partial \alpha_1}\left(\ln\left[\prod_{\mathbf{y}=1}^{N} P[d(\mathbf{y})]\right]\right) \\
&= \frac{\partial}{\partial \alpha_1} \sum_{\mathbf{y}=1}^{N}\left[\frac{d(\mathbf{y})\ln[\alpha_1 h(\mathbf{y}-\mathbf{x}_1) + \alpha_2 h(\mathbf{y}-\mathbf{x}_2) + b_n] - \alpha_1 h(\mathbf{y}-\mathbf{x}_1) - \alpha_2 h(\mathbf{y}-\mathbf{x}_2) - b_n}{\ln[d(\mathbf{y})!]}\right] \\
&= \sum_{\mathbf{y}=1}^{N}\left[\frac{d(\mathbf{y})h(\mathbf{y}-\mathbf{x}_1)}{\alpha_1 h(\mathbf{y}-\mathbf{x}_1) + \alpha_2 h(\mathbf{y}-\mathbf{x}_2) + b_n} - h(\mathbf{y}-\mathbf{x}_1)]\right] \\
&= \sum_{\mathbf{y}=1}^{N}\left[\frac{d(\mathbf{y})h(\mathbf{y}-\mathbf{x}_1)}{\alpha_1 h(\mathbf{y}-\mathbf{x}_1) + \alpha_2 h(\mathbf{y}-\mathbf{x}_2) + b_n}\right] - \sum_{\mathbf{y}=1}^{N}[h(\mathbf{y}-\mathbf{x}_1)] .
\end{aligned}
$$

(3.23)

As has been stated previously, regardless of how it is shifted, the sum of the normalized PSF over all pixels is equal to unity, $\sum_{\mathbf{y}=1}^{N}[h(\mathbf{y}-\mathbf{x}_1) = 1$, resulting in:

$$
1 = \sum_{\mathbf{y}=1}^{N}\left[\frac{d(\mathbf{y})h(\mathbf{y}-\mathbf{x}_1)}{\alpha_1 h(\mathbf{y}-\mathbf{x}_1) + \alpha_2 h(\mathbf{y}-\mathbf{x}_2) + b_n}\right].
$$

(3.24)

In similar fashion of solving for α_0 in Section 3.1.2, we can create a Picard iteration by multiplying both sides by α_1 noting that the right hand side of α_1 is the $n+1$ iteration where n is the iteration index. The same process will give us an equation for α_2, so we have:

$$
\alpha_{1(n+1)} = \alpha_{1(n)} \sum_{\mathbf{y}=1}^{N}\left[\frac{d(\mathbf{y})h(\mathbf{y}-\mathbf{x}_1)}{\alpha_{1(n)} h(\mathbf{y}-\mathbf{x}_1) + \alpha_{2(n)} h(\mathbf{y}-\mathbf{x}_2) + b_n}\right],
$$

(3.25)

$$
\alpha_{2(n+1)} = \alpha_{2(n)} \sum_{\mathbf{y}=1}^{N}\left[\frac{d(\mathbf{y})h(\mathbf{y}-\mathbf{x}_2)}{\alpha_{1(n)} h(\mathbf{y}-\mathbf{x}_1) + \alpha_{2(n)} h(\mathbf{y}-\mathbf{x}_2) + b_n}\right].
$$

(3.26)

Given we have already found a valid value for $\mathbf{x}_1$ and $\mathbf{x}_2$ by solving 3.21, as we iterate through Equations 3.25 and 3.26, $\alpha_{1(n)} h(\mathbf{y}-\mathbf{x}_1) + \alpha_{2(n)} h(\mathbf{y}-\mathbf{x}_2) + b_n$ will converge on $d(\mathbf{y})$ since the right side is a contraction mapping, thus, Equations 3.25 and 3.26 will converge to:

$$
\alpha_{1(n+1)} = \alpha_{1(n)} \sum_{\mathbf{y}=1}^{N}[h(\mathbf{y}-\mathbf{x}_1)]
$$

(3.27)

37

$$\alpha_{2(n+1)} = \alpha_{2(n)} \sum_{\mathbf{y}=1}^{N} [h(\mathbf{y} - \mathbf{x}_2)].$$ (3.28)

Again, no matter how the normalized PSF, $h(\mathbf{y})$, is shifted around the sum over all pixels will be unity by definition, thus, $\sum_{\mathbf{y}=1}^{N} [h(\mathbf{y} - \mathbf{x}_1)] = \sum_{\mathbf{y}=1}^{N} [h(\mathbf{y} - \mathbf{x}_2)] = 1$. Once the difference between the old and new alphas are within a desired value the iterative process ends and the final log-likelihood can be calculated using the last values of $\alpha_{1(n+1)}$ and $\alpha_{2(n+2)}$ as well as the $\mathbf{x}_1$ and $\mathbf{x}_2$ values determined during the first iteration of Equation 3.21 by plugging all these values back into 3.21. This final log-likelihood value will be compared with the value found from hypothesis one to make a determination as to weather the image, $d(\mathbf{y})$ was the result of a single point source or a binary source.

3.2 Software implementation

Software implementation was accomplished using Matlab™. The following subsections will provide a description of software implementation considerations to maximize detection while minimizing false alarm rates and processing time.

3.2.1 Point source threshold.

One of the first tests is to determine if an image contains a high enough signal to noise ratio to be considered for hypothesis one and two. If an image contains no pixels above a calculated threshold it is ignored from further processing. This threshold is based on the detected background noise as well as a pre-determined tolerance for false positive point sources. The probability that a pixel which contains only background noise is falsely measured as a valid signal is:

$$P_{\text{false signal}} = 1 - \sum_{k=0}^{t} \frac{(b_n)^k e^{-b_n}}{k!}.$$ (3.29)

For the simulated results provided in this thesis the probability of a false signal was set to, $P_{\text{false signal}} = 1 \times 10^{-8}$. What remains is to solve for the threshold variable, t such that the right side of Equation 3.29 is equal to 1×10^{-8}. This is the first threshold used in implementation and is used for determining which pixels in an image warrant processing.

38

If an image contains no pixels above the threshold, it is determined to be hypothesis zero, no objects detected.

3.2.2 zero point source implementation.

As soon as the detected image, $d(\mathbf{y})$, is captured, cropped and ready for detection processing the median background noise can be calculated. The results for this background noise estimate, referred to as b_n throughout this thesis, are fed into the first threshold discussed in the previous subsection. If an image to be processed contains no pixels that exceed the background noise threshold they are ignored and it is assumed that hypothesis zero is correct. In this way the image does not need to be processed for hypothesis one and two if it meets the criteria for being hypothesis zero, that is when the image is assumed to have no point sources.

3.2.3 Single point source implementation.

Given we have already calculated the background noise, b_n, and have a valid PSF, $h(\mathbf{y})$, we can implement the log-likelihood equation for hypothesis one, 3.12, and the $\alpha_{0(n+1)}$ Equation, 3.16. The results of these two algorithms will be the most likely intensity and location of a single point source that could produce the detected image, $d(y)$. It will also produce a numerical value, the log-likelihood, which will be compared to hypothesis two to determine detection of a binary. As derived in Section 3.1.2, the log-likelihood for hypothesis one is:

$$LL_{h1} = \sum_{\mathbf{y}=1}^{N} \left[d(\mathbf{y}) \left(\ln[\alpha_0 h(\mathbf{y} - \mathbf{x}_0) + b_n] \right) - \alpha_0 h(\mathbf{y} - \mathbf{x}_0) - b_n - \ln[d(\mathbf{y})!] \right].$$

To improve the computational efficiency, the term, $\ln[d(\mathbf{y})!]$ is dropped. This will not impact the final decision because it sums to the same value in both hypothesis one and two. The final form of LL_{h1} that will be implemented in code is:

$$LL_{h1} = \sum_{\mathbf{y}=1}^{N} \left[d(\mathbf{y}) \left(\ln[\alpha_0 h(\mathbf{y} - \mathbf{x}_0) + b_n] \right) - \alpha_0 h(\mathbf{y} - \mathbf{x}_0) - b_n \right]. \tag{3.30}$$

Given the above information, the implementation process is as follows,

1. Calculate the estimate for α_0 using Equation 3.13.

2. Calculate the log-likelihoods for hypothesis one, Equation 3.30, using the estimate for α_0 and cycling through valid source locations governed by $\mathbf{x}_0$.

3. Find the $\mathbf{x}_0$ associated with the highest log-likelihood value.

4. Use the $\mathbf{x}_0$ found in step 3 to find a more accurate value of α_0, denoted $\alpha_{0(n+1)}$, where n is the number of iterations used to converge on a value where $\alpha_{0(n+1)} = \alpha_{0(n)}$ using Equation 3.16.

5. Using the values of $\alpha_{0(n+1)}$ and $\mathbf{x}_0$ calculated above, calculate the log-likelihood of hypothesis one a final time. This is the value used in comparison with hypothesis two results.

Not all pixels need to be evaluated as potential locations of the point source, $\mathbf{x}_0$. Only pixels in a 20 by 20 grid surrounding the brightest pixel in a given image, $d(y)$ are evaluated. This step significantly reduced the processing time.

3.2.4 Two point source implementation.

Implementation of the binary or two point source hypothesis is similar to hypothesis one. It is worth repeating for completeness. Given the background noise, b_n, and valid PSF, $h(\mathbf{y})$, we can implement hypothesis two log-likelihood Equation 3.21, as well as the $\alpha_{1(n+1)}$ and $\alpha_{2(n+1)}$ Equations 3.27 and 3.28. As derived in Section 3.1.3, the log-likelihood for hypothesis two is:

$$LL_{h2} = \sum_{\mathbf{y}=1}^{N} \left[\frac{d(\mathbf{y})\ln[\alpha_1 h(\mathbf{y} - \mathbf{x}_1) + \alpha_2 h(\mathbf{y} - \mathbf{x}_2) + b_n] - \alpha_1 h(\mathbf{y} - \mathbf{x}_1) - \alpha_2 h(\mathbf{y} - \mathbf{x}_2) - b_n}{\ln[d(\mathbf{y})!]} \right].$$

To improve the computational efficiency, the term, $\ln[d(\mathbf{y})!]$ is dropped. This will not impact the final decision because it sums to the same value in hypothesis zero, one and

two. The final form of LL_{h2} that will be implemented in code is:

$$\sum_{\mathbf{y}=1}^{N} [d(\mathbf{y}) \ln[\alpha_1 h(\mathbf{y} - \mathbf{x}_1) + \alpha_2 h(\mathbf{y} - \mathbf{x}_2) + b_n] - \alpha_1 h(\mathbf{y} - \mathbf{x}_1) - \alpha_2 h(\mathbf{y} - \mathbf{x}_2) - b_n]. \quad (3.31)$$

Given the above information, the implementation process is the same as hypothesis one the primary difference being the need to solve for two point source intensities and locations instead of one. The process is as follows,

1. Calculate the estimate for α_1 and α_2 using Equation 3.22.

2. Calculate the log-likelihoods for hypothesis two, Equation 3.31, using the estimates for α_1 and α_2 from step one and cycling through valid source locations governed by $\mathbf{x}_1$ and $\mathbf{x}_2$. This requires a quadruple iteration loop.

3. Find the $\mathbf{x}_1$ and $\mathbf{x}_2$ associated with the highest log-likelihood value.

4. Use the $\mathbf{x}_1$ and $\mathbf{x}_2$ found in step three to find a more accurate value of α_1 and α_2, denoted $\alpha_{1(n+1)}$ and $\alpha_{2(n+1)}$, where n is the number of iterations used to converge on a value where $\alpha_{1(n+1)} = \alpha_{1(n)}$ and $\alpha_{2(n+1)} = \alpha_{2(n)}$ using Equation 3.27 and Equation 3.28.

5. Using the values of $\alpha_{1(n+1)}$ and $\alpha_{2(n+1)}$ from step four and $\mathbf{x}_1$ and $\mathbf{x}_2$ from step three, calculate the log-likelihood of hypothesis two one final time. This is the value used in comparison with hypothesis one results.

Again, not all pixels need to be evaluated as potential locations of the point sources, $\mathbf{x}_1$ and $\mathbf{x}_2$. Only pixels in a 20 by 20 grid surrounding the brightest pixel in a given image, $d(y)$ are evaluated. In addition, pixel locations in the subset that did not exceed the estimated background noise were ignored. These steps significantly reduced the processing time.

3.2.5 Decision process.

It is important to note that all simulated tests used short exposure generated images for both the detected image and the PSF. The measured images used are long exposure

41

images. An area for further testing is to compare detection techniques using simulating long exposure images in various configurations.

Given the log-likelihood values found from implementing the hypothesis one and two algorithms, the task of making a correct decision is the next step. One would think that simply comparing the results would give the best decision as to weather or not a binary exists. However, because hypothesis two has more degrees of freedom its log-likelihood value is almost always higher than hypothesis one. A bias is needed to give more weight to hypothesis one. If τ is the bias, the following equation demonstrates the decision logic implemented in simulation:

$$LL_{H2} > LL_{H1} + \tau. \tag{3.32}$$

Finding the value for τ that increases the probability of correct detection and reduces the probability of false alarm is a key point of the simulation tests. Chapter four will provide the results of several tests that show how properly choosing τ can impact false alarm and detection requirements.

Another important decision criteria is how close can two objects be in the detection plane and be considered two objects. Some deep space surveillance telescopes are under sampled. A single object that is smaller than a pixel in the detection plane might appear as two adjacent pixels due to atmospheric blurring or the orientation of the telescope. For this reason, the detection code will ignore the eight pixels immediately surrounding the brightest pixel in the area of interest. If this step is not done, the Probability of False Alarm (P_{fa}) rate goes up to around 40% due to the single point source often being split between two adjacent pixels as described. This pixel elimination induces a requirement that a binary will only be detected if there is at least one pixel of separation between the point sources. This may not be necessary depending on the image quality. For instance, this restriction was not needed on the measured images used in this thesis. An area of future research is to explore using sub-pixel processes to allow binaries to be detected with high

confidence when two bright pixels are adjacent.

Applying the bias correction τ and adjacent pixel restriction as described above, the final step is to compare the log-likelihoods. The most likely hypothesis is returned as the final decision of the code. Chapter four will show a number of results using various initial conditions. The next section will discuss how the simulations for those results were conducted.

The detection technique used for the images processed by the correlation method took the brightest pixel and then, based on it's intensity, looked for another pixel with brightness above a variable threshold. The threshold for the second pixel was determined by keeping the false alarm rate below 10%. Again, the restriction on adjacent pixels being valid solutions was enforced.

3.3 Simulation test model

An in-focus telescope was simulated to test various seeing parameters and thresholds using the multi-hypothesis implementation previously described. The diameter, D, and focal length are 1 meter. The detection plane consisted of $N \times N$ samples, where $N = 128$. The wavelength of light, λ, was set to, $\lambda = 0.5\,\mu$m. Photon arrival is assumed to be governed by Poisson statistics and is applied to the intensities calculated at each point in the detection plane. As with most simulated tests, the number of trials is important. For each of the simulated test, 200 random images were generated for each background noise, seeing condition, and binary/point source intensity. The next few subsections will provide more detail on atmospheric settings, how the threshold, source intensities, and seeing conditions were simulated, and how results were quantified.

3.3.1 Modeling atmospheric effects.

As described in Section 2.1.1, randomly generated phase screens using Zernike polynomials were used for all simulation models. Again, as was previously described, given an aperture diameter, D, Fried seeing parameter, r_0, and how many polynomial

expansions are desired, a random phase screen can be produced using Equations 2.1-2.9 found in Chapter 2. The number of Zernike polynomials used will dictate the amount of higher order aberrations that the model will be able to reproduce. For the simulations conducted for this thesis 85 Zernike polynomials were used to model atmospheric distortion. The diameter of the aperture was set to, $D = 1$ meter. The Fried seeing parameter, r_0, is one of the variables modulated during different tests, the results of which are provided in Chapter 4.

3.3.2 Test variables.

For the simulated binary tests, two point sources were modeled being separated by the equivalent of one pixel in the detection plane. The parameters for the tests were as follows,

1. The Fried seeing parameter, r_0. Adjusting this directly influences the amount of atmospheric turbulence created by the Zernike phase screen generator. A larger r_0, given in meters, corresponds with better seeing conditions and thus lower atmospheric turbulence.

2. Switching between one or two point sources to demonstrate both correctly detecting when two point sources are present and also properly detecting when only a single point source was simulated.

3. Point source intensity and intensity variance between binary points. Both the overall intensity and the intensity between the two point sources was modulated to show performance falloff and error rates as light levels drop and/or light variance increases between points.

These three items–seeing conditions, a single vs. binary source, and light intensity for the source(s) were the only variables changed to produce the simulated images used for testing. The only variable in the detection phase of the code is τ, which controls the weighted bias for hypothesis one to counteract the advantage hypothesis two has in degrees of freedom.

3.3.3   Performance measurements for simulated data.

By adjusting the three variables described in the previous section, namely, seeing conditions, one or two point sources, and source intensity, simulated single-frame short exposure images are produced. The multi-hypothesis algorithm processes these simulated images and produces log-likelihoods for hypothesis one and two. A decision is then made as to which hypothesis is more likely. Two key metrics are Probability of False Alarm, P_{fa}, and Probability of Detection, P_D. The results found in Chapter 5 will show plots for the probabilities of detection and false alarm as these different variables are adjusted. The goal is to form conclusions on what kind of performance can be expected given different source patterns in various seeing conditions.

3.3.4   Simulated comparison model.

In an effort to show how image reconstruction techniques might perform in the same simulations, an imaging by correlation process with its corresponding result data has been implemented. The simulated images are the same as for the multi-hypothesis model. For detection, a simple logic process is used to decide if the reconstructed image contains one or two objects in the area of interest above a threshold set to reduce the false alarm rate. Similar to the multi-hypothesis method, pixels immediately surrounding the brightest pixel in the region of interest are ignored to lower the false alarm rate considerably. The imaging by correlation technique implemented is outlined in Chapter 2 Section 2.1.3. Because the simulation tests a single short exposure image, the intensity of the source is increased to allow the imaging by correlation method to get into a range in which it can reconstruct a binary. Another note is the use of a low D/r_0 value, it was also necessary to lower this value to obtain reasonable results. The imaging by correlation method typically uses multiple images of the same object to achieve quality results. However, to compare it to the multi-hypothesis method, which in these simulations only use single short exposure

images, atmospheric effects are reduce to compensate for lack of multi-frame imaging. The low D/r_0 can be effectively achieved by an adaptive optic system.

3.4   Measured data test model

A large data set of images taken of various geosynchronous objects by the Space Surveillance Telescope (SST) is examined in this section. In some of the images, it is clear that a dim star moves close to the stationary object–even where they appear to be a single object. This provides a good set of images to demonstrate potential real-world performance of the multi-hypothesis detection algorithms. The measured data test follows these steps,

1. import measured data image to be processed for detection

2. import measured data images to be used to calculate estimated PSF

3. Calculate estimate PSF based on images of a single point taken near to the time and location of the image to be processed for detection.

4. Calculate the estimate background noise level of the image to be processed for detection.

5. process the image for detection through the multi-hypothesis algorithm. Return the log-likelihood of both hypothesis one and two.

The results of this process for the images previously described are provided in Chapter 4.

3.4.1   Description of measured data.

The measured data used in this test was taken by the SST, which is a Defense Advanced Research Projects Agency (DARPA) program designed to detect space debris in earth's orbit (see http://www.darpa.mil/Our_Work/TTO/Programs/Space_Surveillance_Telescope_(SST).aspx for more information). The images used in this thesis were taken in 2012 and focus on the ANIK-F1 and ANIK-F1R geosynchronous communications satellites.

3.4.2 Deriving a valid PSF.

As enumerated above, a valid PSF is key to estimating the most likely location and intensity of the point source(s). This is done by taking multiple images at around the same time and location as the image being processed for detection. The average PSF over these multiple images is when running the multi-hypothesis algorithm. One of the major assumptions of this method is the ability to obtain a valid point spread function.

3.4.3 Determining success of measured data test.

The set of images used for this test shows a satellite in the center while a dim star moves into the picture and eventually right next to the satellite. The detection algorithm should properly detect the single object until the second object, the star, moves into the region of interest. How well it performs when the satellite and the star look like a single point is of particular interest. The results of this test are reported in Chapter 4.

IV.   Results

T HE goal of this chapter is to provide test results using both simulated and measured data in a way that is easy to compare and digest. Please refer to Chapter 3 of this thesis for a more detailed look at the setup of the simulations. The basic simulation setup is to generate images using phase screens to represent various amounts of atmospheric distortion on binary points separated by a single pixel width. Average background noise and atmospheric turbulence are varied by noted amounts in each section. The first section will look at the relationship between the Probability of Detection (P_D) and P_{fa} as governed by a bias variable. The second section will compare the multi-hypothesis method to an implementation of imaging by correlation as described in Chapter 3. The third section will look at results as real measured images are evaluated by the multi-hypothesis detection algorithm.

4.1   Multi-hypothesis binary detection simulation results

Test parameters for calculating the P_D and P_{fa} are as follows,

1. Three different binary sources were used. All with a detection-plane pixel-width of separation between points.

    A. First, both points at 500 photons of intensity.

    B. Second, one point source at 1000 and one at 500 photons of intensity.

    C. Third, both points at 1000 photons of intensity.

2. Three different point sources were used to measure P_{fa} related to the P_D of similar intensity.

    A. First, a single point at 1000 photons of intensity corresponding to the binary points of 500 photons each.

48

B. Second, a single point at 2000 photons of intensity corresponding with the binary points of 1000 photons each.

C. Third, a single point at 1500 photons each corresponding with the binary points of 1000 and 500.

3. 200 random images were generated for each binary source for each combination of D/r_0 and background noise level.

4. D/r_0 levels simulated, $D/r_0 = [1.25, 1.43, 1.67, 2, 2.5, 3.33, 5, 10]$.

5. Background levels simulated, $noise = [1, 2, 3, 4, 5, 6, 7, 8]$ photons.

6. The center of mass of each simulated image was centered and a pixel window of $128x128$ was sent to the algorithm for processing.

7. A normalized PSF was simulated corresponding to each simulated image passing through the same atmospheric phase screen.

8. The assumption that there must be at least one pixel of separation between the binary points was enforced in the code, so adjacent pixels were not considered as valid hypothesis two solutions. This reduces the false alarm rate.

It should be noted that the decision to use Freid seeing parameters above $0.3m$ is made to simulate conditions when atmospheric distortion is justified by the effect of adaptive optics which partially compensate for the effects of atmospheric turbulence.

4.1.1 Image generation.

The following are a sample of the 76,800 images generated and processed to estimate the probability of detection and false alarm for various noise and seeing conditions. The first, Figure 4.1, shows samples of simulated short exposure binaries, the second, Figure 4.2, single point sources. The amount of background noise and atmospheric conditions are noted under each sample image.
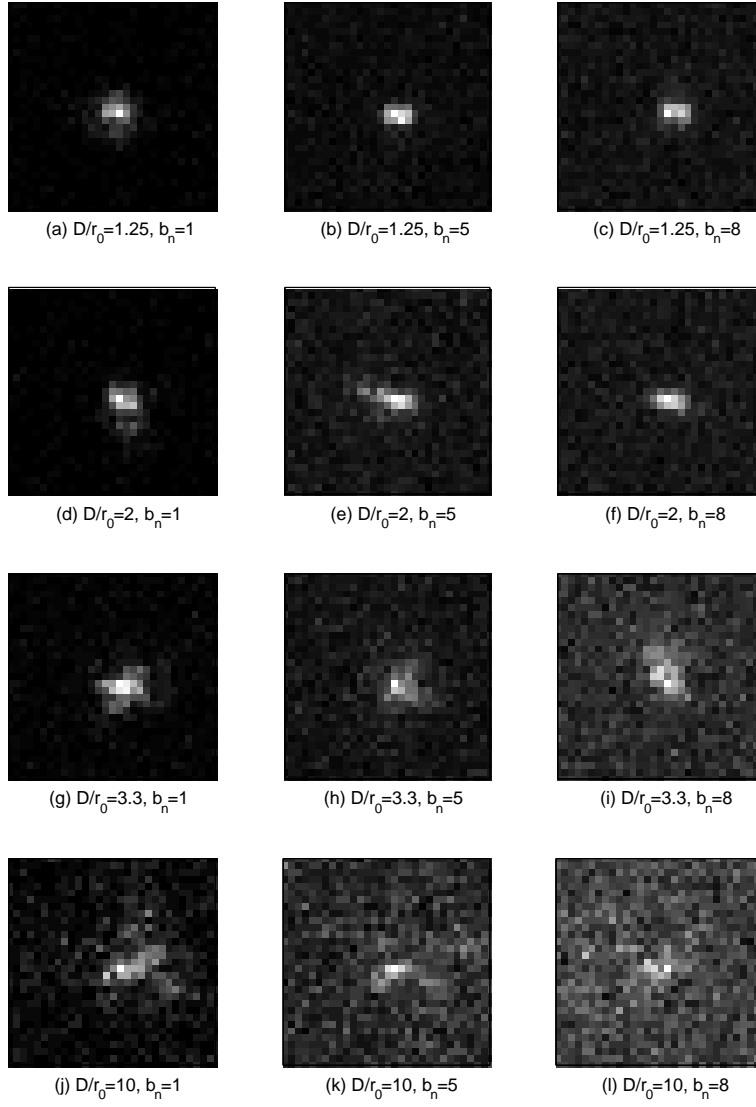
Figure 4.1: Sample simulated detected images of binary source with 500 photons for each point. Samples taken for various background noise and D/r_0 values as given next to each image. Zoomed in to 31x31 pixels.
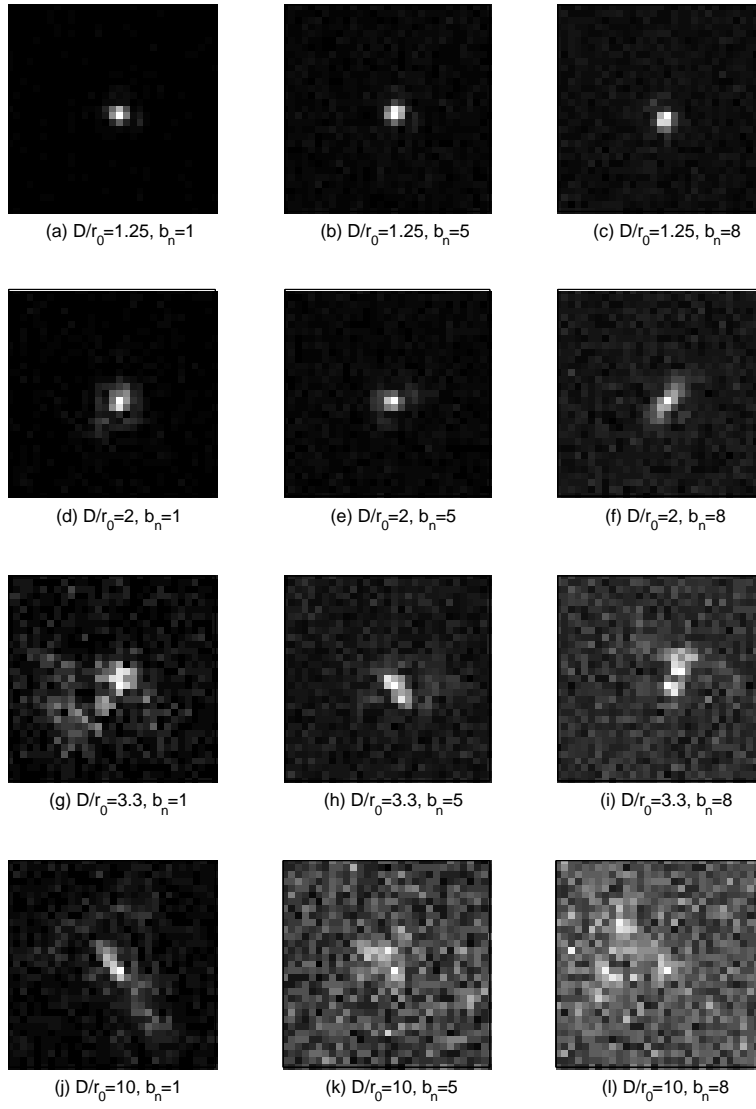
Figure 4.2: Sample simulated detected images of single point sources used in calculating false alarm rates. Samples taken for various background noise and D/r_0 values as given next to each image. Zoomed in to a 31x31 pixel area.

4.1.2 Log-likelihood bias correction.

Hypothesis two has an advantage in the form of more degrees of freedom to fit two shifted and scaled point spread functions to the detected image. If LL_{H1} and LL_{H2} are the log-likelihood results of hypothesis one and two respectively then:

$$LL_{H2} > LL_{H1} + \tau, \tag{4.1}$$

where τ is controls how much bias to give to hypothesis one to reduce the false alarm rates. For the simulation results of this thesis, a maximum false alarm rate of 10% was set and τ adjusted accordingly. The resulting value for τ for each test is as follows,

1. Test one, binary of 500 photons each and a single point source of 1000 photons. $\tau = 36$.

2. Test two, binary of 1000 and 500 photons and a single point source of 1500 photons. $\tau = 60$.

3. Test three, binary of 1000 photons each and a single point source of 2000 photons. $\tau = 88$.

The next several subsections will provide the resulting P_D and P_{fa} tables corresponding with each test.

4.1.3 Probability of Detection (P_D) sample results.

The P_D tables in this section provide data on how often the multi-hypothesis algorithm successfully detected a binary averaged over 200 trials under each combination of background noise and D/r_0. Background noise increases moving vertically and D/r_0 increases moving horizontally in each table. Each of the three tables in this section are from a different combination of binary sources. The first is from a binary whose simulated intensity at the aperture plane, prior to applying the atmosphere and noise, are each 500 photons. The second is a binary where one point is 1000 and one is 500 photons. The last table provides the P_D results when the binary points each have 1000 photons.

53

Table 4.1: Probability of Detection (P_D) results using binary source with 500/500 photons.

P_D results, binary source 500/500 photons									
		atmospheric seeing, D/r_0							
		1.25	1.43	1.67	2.00	2.50	3.33	5.00	10.00
added background noise in photons	1	100%	100%	100%	100%	100%	100%	99.5%	96.5%
	2	100%	99.5%	99.5%	98%	92.5%	92%	78.5%	26%
	3	93.5%	85%	88.5%	81.5%	67.5%	48%	20%	2.5%
	4	38.5%	39.5%	27%	21.5%	12%	8%	2.5%	0%
	5	4%	5%	2.5%	1.5%	2%	0.5%	0%	0%
	6	0%	0%	0%	0.5%	0%	0%	0%	0%
	7	0%	0%	0%	0%	0%	0%	0%	0%
	8	0%	0%	0%	0%	0%	0%	0%	0%

Table 4.2: Probability of Detection (P_D) results using binary source with 1000/500 photons.

P_D **results, binary source 1000/500 photons**									
		atmospheric seeing, D/r_0							
		1.25	1.43	1.67	2.00	2.50	3.33	5.00	10.00
added background noise in photons	1	100%	100%	100%	100%	100%	100%	100%	97.5%
	2	100%	100%	100%	100%	98%	90.5%	67.5%	10.5%
	3	97%	95%	92.5%	85%	65.5%	44.5%	8%	0%
	4	30%	26.5%	21.5%	15%	9%	2%	0%	0%
	5	0%	0%	0%	0%	0%	0%	0%	0%
	6	0%	0%	0%	0%	0%	0%	0%	0%
	7	0%	0%	0%	0%	0%	0%	0%	0%
	8	0%	0%	0%	0%	0%	0%	0%	0%

Table 4.3: Probability of Detection (P_D) results using binary source with 1000/1000 photons.

P_D **results, binary source 1000/1000 photons**									
		atmospheric seeing, D/r_0							
		1.25	1.43	1.67	2.00	2.50	3.33	5.00	10.00
added background noise in photons	1	100%	100%	100%	100%	100%	100%	100%	99%
	2	100%	100%	100%	99.5%	100%	97.5%	87%	38%
	3	98%	97.5%	97.5%	92%	85.5%	73.5%	31.5%	3.5%
	4	71%	64.5%	61%	47%	33%	18.5%	6%	0%
	5	9%	4%	4%	6%	5%	0.5%	0%	0%
	6	0%	0%	0%	0%	0.5%	0%	0%	0%
	7	0%	0%	0%	0%	0%	0%	0%	0%
	8	0%	0%	0%	0%	0%	0%	0%	0%

4.1.4 Probability of false alarm (P_{fa}) simulation results.

The P_{fa} tests entail processing single point sources at similar intensity to a corresponding binary sources as described in Chapter 3. A maximum P_{fa} of 10% was enforced as previously stated. Decreasing the P_{fa} will also decrease the detection rate. The following three tables will follow the style and format of the P_D tables using the same scale and parameters, the only difference being the actual processed images. The first table will show P_{fa} results using a point source with 1000 photons of intensity in the aperture plane, again, prior to diffraction, added noise and atmospheric blurring. The second table will show results when using a point source of 1500 photons and the final table contains the results when a point source of 2000 photons was used in image generation.

Table 4.4: Probability of False Alarm (P_{fa}) results using point source with 1000 photons.

		P_{fa} **results, point source with 1000 photons**							
		atmospheric seeing, D/r_0							
		1.25	1.43	1.67	2.00	2.50	3.33	5.00	10.00
added background noise in photons	1	0%	0%	0.5%	0%	2%	5%	8.5%	8%
	2	0%	0%	0%	0%	0%	0.5%	0%	0%
	3	0%	0%	0%	0%	0%	0%	0%	0%
	4	0%	0%	0%	0%	0%	0%	0%	0%
	5	0%	0%	0%	0%	0%	0%	0%	0%
	6	0%	0%	0%	0%	0%	0%	0%	0%
	7	0%	0%	0.5%	0%	0%	0%	1%	0%
	8	0.5%	0%	0.5%	0%	0%	0%	0%	0%

Table 4.5: Probability of False Alarm (P_{fa}) results using point source with 1500 photons.

P_{fa} results, point source with 1500 photons								
		atmospheric seeing, D/r_0						
		1.25	1.43	1.67	2.00	2.50	3.33	5.00	10.00
added background noise in photons	1	0%	0%	0%	0%	1%	1.5%	3%	8%
	2	0%	0%	0%	0%	0%	0%	0%	0%
	3	0%	0%	0%	0%	0%	0%	0%	0%
	4	0%	0%	0%	0%	0%	0%	0%	0%
	5	0%	0%	0%	0%	0%	0%	0%	0%
	6	0%	0%	0%	0%	0%	0%	0%	0%
	7	0%	0%	0%	0%	0%	0%	0%	0%
	8	0%	0%	0%	0%	0%	0%	0%	0%

Table 4.6: Probability of False Alarm (P_{fa}) results using point source with 2000 photons.

P_{fa} results, point source with 2000 photons								
		atmospheric seeing, D/r_0						
		1.25	1.43	1.67	2.00	2.50	3.33	5.00	10.00
added background noise in photons	1	0%	0%	0%	0%	0.5%	2%	4%	9%
	2	0%	0%	0%	0%	0%	0%	0%	0%
	3	0%	0%	0%	0%	0%	0%	0%	0%
	4	0%	0%	0%	0%	0%	0%	0%	0%
	5	0%	0%	0%	0%	0%	0%	0%	0%
	6	0%	0%	0%	0%	0%	0%	0%	0%
	7	0%	0%	0%	0%	0%	0%	0%	0%
	8	0%	0%	0%	0%	0%	0%	0%	0%

4.1.5 P_D and P_{fa} result summary.

The P_D depends on the log-likelihood of hypothesis two being greater than the log-likelihood of hypothesis one plus a weighting factor, τ. The weighting factor was set in such a way that the P_{fa} was kept under 10%, for a given test which cycled through various background noise and atmospheric imaging conditions. The results of this section show that this multi-hypothesis algorithm can correctly detect binaries under a wide range of conditions while maintaining a low false alarm rate. However, as seeing conditions fall below $D/r_0 = 5$ and noise values rise above $B_{noise} = 4$ photons, the detection under these simulated binaries drops off. As expected, the higher the signal to noise the better overall detection. The tests where a binary with 1000 and 500 photons of intensity was used show that the multi-hypothesis algorithm can differentiate a dim object next to a brighter object. These results also demonstrate that using adaptive optics and/or image post-processing enhancements that lower the effective D/r_0 and raise the signal to noise ratio will greatly improve the detection rate while maintaining a low false alarm rate. The next section will compare some of the results above to a detection algorithm used on images enhanced using speckle interferometry.

4.2 Comparison with imaging by correlation technique

This section will describe the results obtained when running binary and single point images with various amounts of noise and atmospheric blur through the detection algorithms as described in Chapter 3. The imaging by correlation technique attempts to reconstruct the single short exposure image around a small group of pixels that should contain either a binary or point source. Then a threshold, which has been set to maintain a false alarm rate below 10%, determines if a binary or single point is contained in the reconstructed image. This is compared to the multi-hypothesis method which calculates the log-likelihoods of a single point or binary in a given image. Both methods keep the P_{fa} below 10% and both enforce the requirement that a binary have at least one pixel of space

between points.

The following are the simulation parameters used in the comparison tests.

1. Three different binary sources were used. All with a pixel-width (in the aperture plane) of separation between points before diffraction and atmospheric blurring.

    A. First, both points at 500 photons of intensity.

    B. Second, one point at 1000 and one at 500 photons of intensity.

    C. Third, both points at 1000 photons of intensity.

2. Three different point sources were used to measure P_{fa} related to the P_D of similar intensity.

    A. First, a single point at 1000 photons of intensity corresponding to the binary points of 500 photons each.

    B. Second, a single point at 1500 photons of intensity corresponding with the binary points of 1000 and 500 photons.

    C. Third, a single point at 2000 photons of intensity corresponding with the binary points of 1000 photons each.

3. 200 random images were generated for each binary source for each combination of D/r_0 and background noise level.

4. D/r_0 levels simulated, $D/r_0 = [1.7, 2.5, 5]$.

5. Background levels simulated, $noise = [1, 2, 3]$ photons.

6. Images were $128x128$ pixels each.

7. A normalized PSF was simulated corresponding to each simulated image passing through the same atmospheric phase screens.

8. The assumption that there must be at least one pixel of separation between the binary points was enforced in the code.

The next subsections will provide the P_{fa} results first and then the P_D results.

4.2.1 *Probability of False Alarm (P_{fa}) comparison results.*

First the P_{fa} comparison results are provided. As has been mentioned before, a ceiling of 10% was enforced. The following three figures will show the P_{fa} as a function of D/r_0 for the different background noise level as well as for each simulated brightness level.
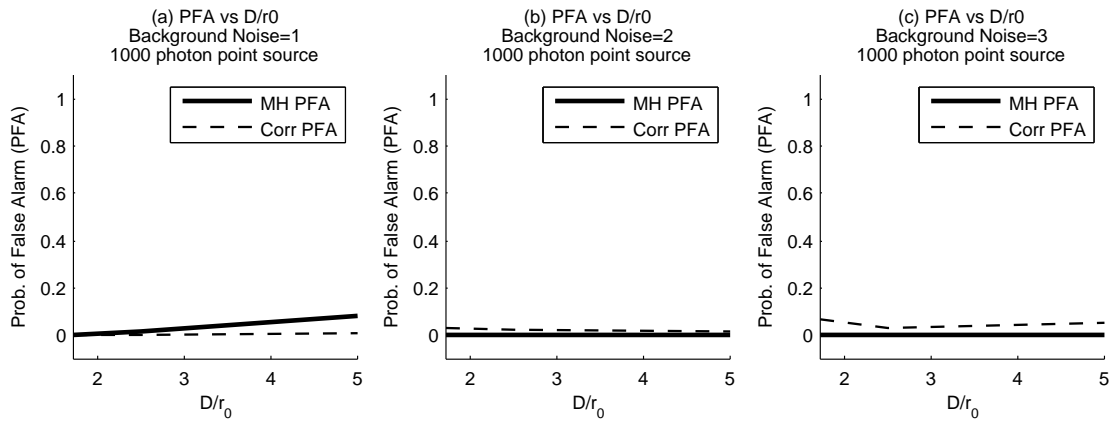

Figure 4.3: False Alarm rate versus D/r_0 for a point source with an intensity of 1000 photons for, (a) background noise level=1, (b) background noise level=2, (c) background noise level=3.
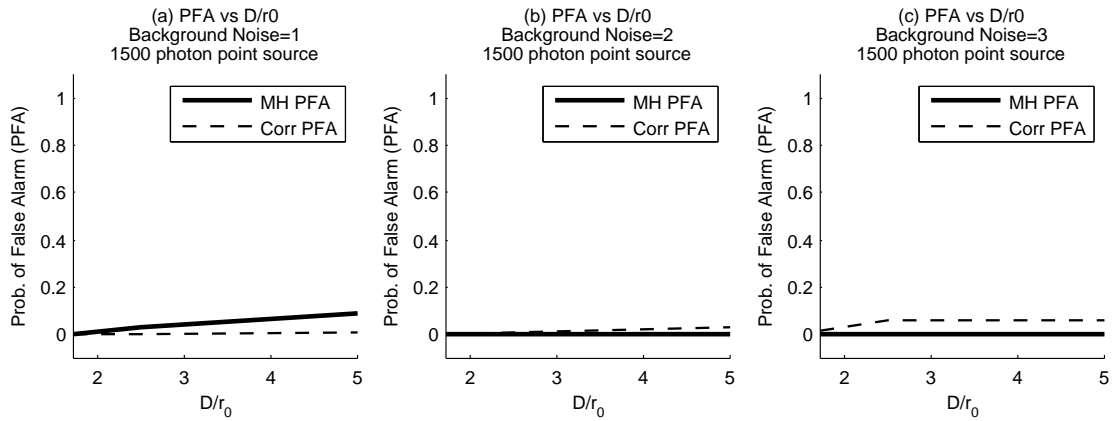
Figure 4.4: False Alarm rate versus D/r_0 for a point source with an intensity of 1500 photons for, (a) background noise level=1, (b) background noise level=2, (c) background noise level=3.
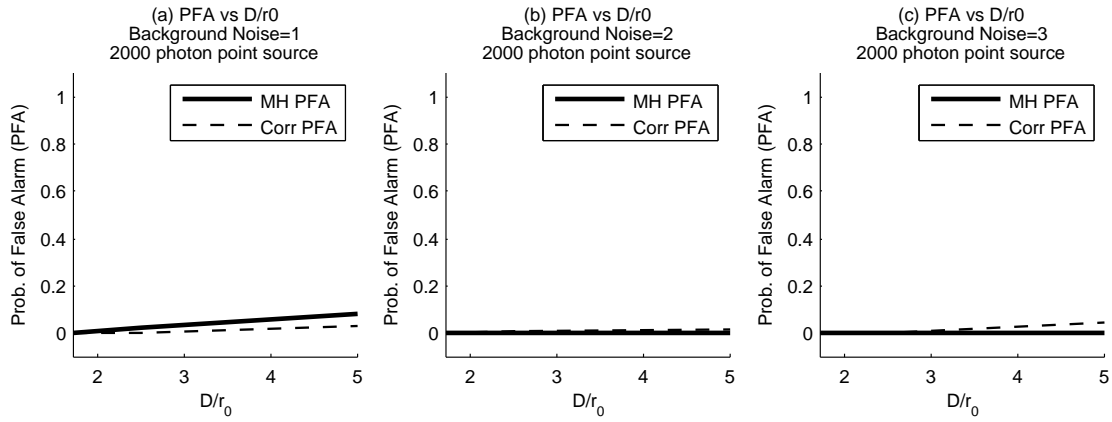

Figure 4.5: False Alarm rate versus D/r_0 for a point source with an intensity of 2000 photons for, (a) background noise level=1, (b) background noise level=2, (c) background noise level=3.

### 4.2.2 Probability of Detection (P_D) comparison results.

This subsection provides the P_D comparison results. Each figure plots the probability of detection versus D/r_0 for various background noise and brightness levels as indicated in each graph. These detection rates are impacted by maximum allowable false alarm rate, as explained in Chapter 3.
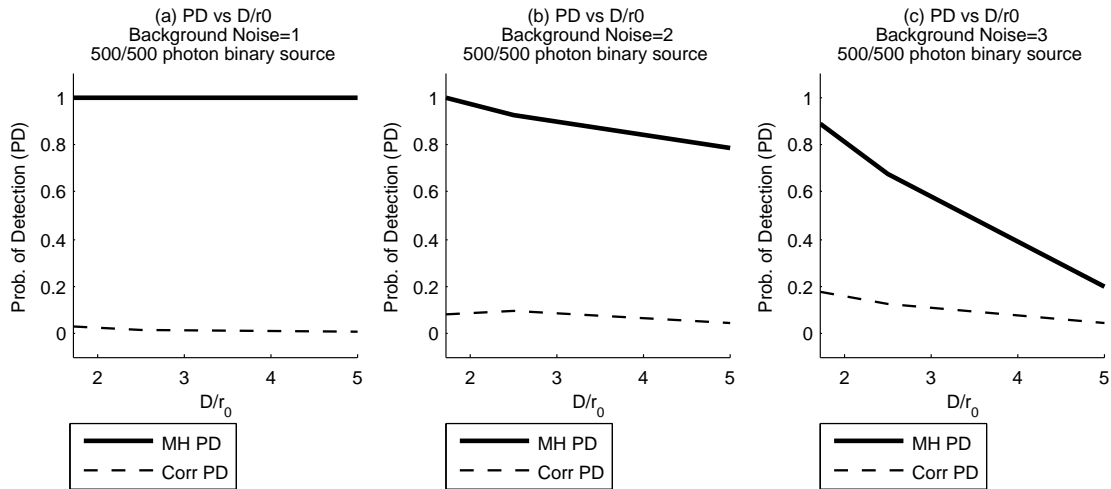
Figure 4.6: Detection rate versus D/r_0 for a binary source with an intensities of 500 and 500 photons for, (a) background noise level=1, (b) background noise level=2, (c) background noise level=3.
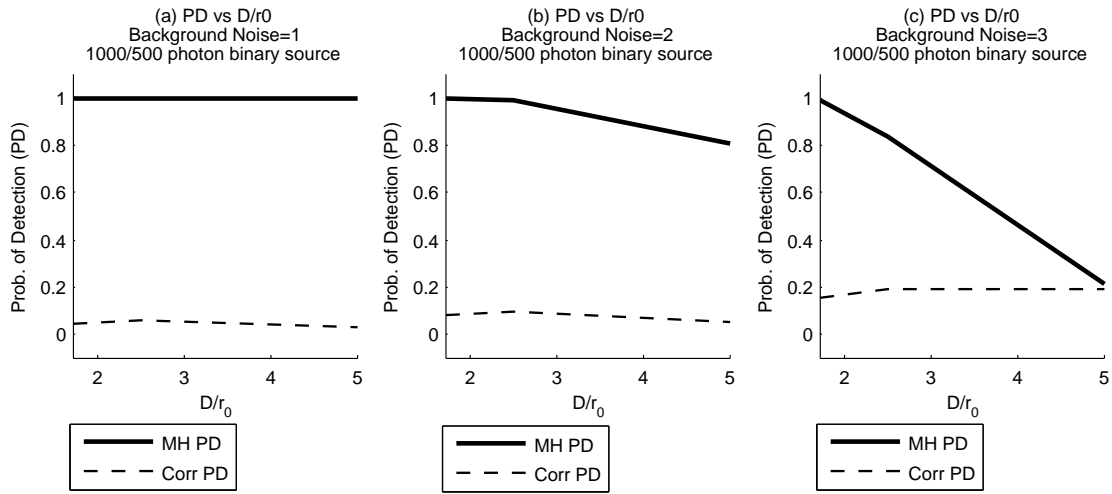
Figure 4.7: Detection rate versus D/r_0 for a binary source with an intensities of 1000 and 500 photons for, (a) background noise level=1, (b) background noise level=2, (c) background noise level=3.
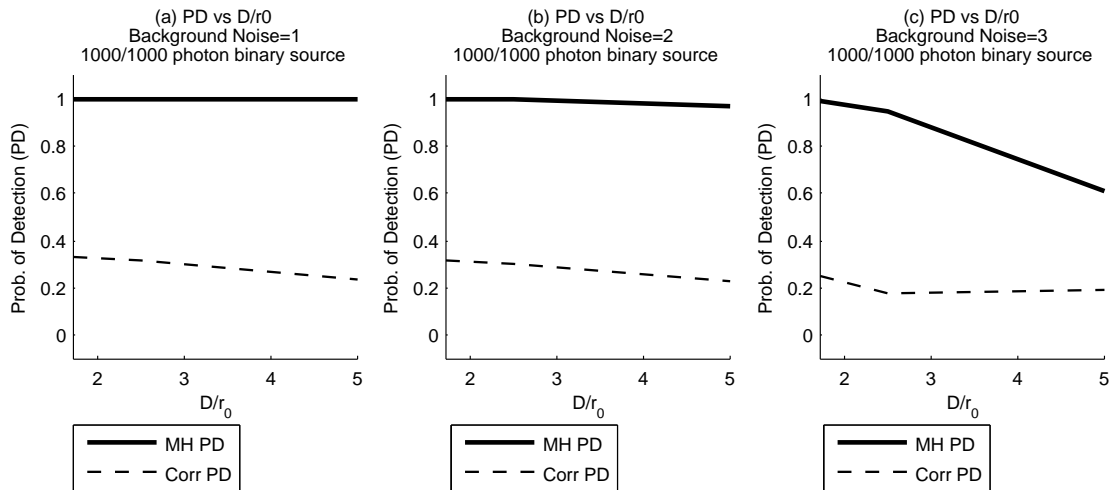
Figure 4.8: Detection rate versus D/r_0 for a binary source with an intensities of 1000 and 1000 photons for, (a) background noise level=1, (b) background noise level=2, (c) background noise level=3.

4.2.3 Comparison result summary.

From the data obtained from the simulation tests, the P_{fa} performance of the imaging by correlation and multi-hypothesis methods are similar. This is due to the enforcement of a common maximum of 10% being enforced on both detection algorithms. The maximum threshold can obviously be increased or decreased depending on the desired false alarm rate.

Looking at the P_D results, it is clear that the multi-hypothesis method, in the given simulated tests, is superior in detection. These positive results demonstrate a significant potential improvement over traditional binary detection methods when that detection is based on a single short exposure image.

4.3 Measured data processing results

As described in Chapter 3, image data was obtained from the DARPA SST. These images were focused on two satellites in Geostationary Earth Orbit (GEO). As the telescope is focused on a satellite in GEO, stars appear to pass by in the background. On a few occasions, a starlight will be right next to the satellite so as to appear to be a single blurry object. This is the scenario that was run through the multi-hypothesis algorithm to see if it correctly detected a single source when the object satellite is the only light source in the frame and then correctly detect a binary as relatively equal intensity starlight moves into the frame and then right next to the satellite. A PSF was estimated by averaging several images where a single point is present around the same time as the images processed for detection. The following four subsections provide the images used and the detection results.

4.3.1 First image: two points spaced far away.

The first image in this sequence of four contains a satellite centered and a star entering the frame on the top. This is clearly a binary and, as expected, hypothesis two had a higher log-likelihood.
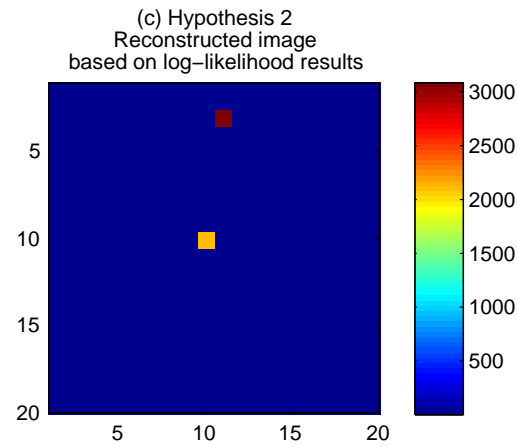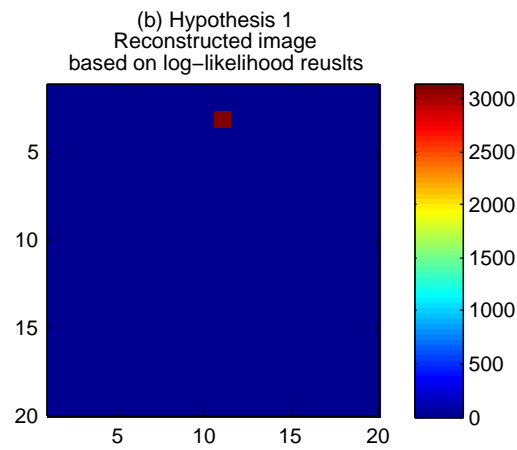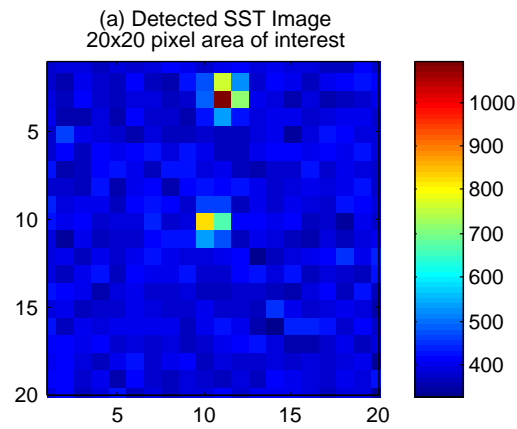
Figure 4.9: First measured image (a) Detected image, (b) Result of hypothesis one, (c) Result of hypothesis two. The log-likelihood of hypothesis two was larger and therefore a binary was detected.

4.3.2 Second image: two points in close proximity.

The second image is of most interest. Here the star from the previous frame has moved right next to the satellite so it would appear as if they are one bright object. The multi-hypothesis algorithm successfully determined that this is a binary.
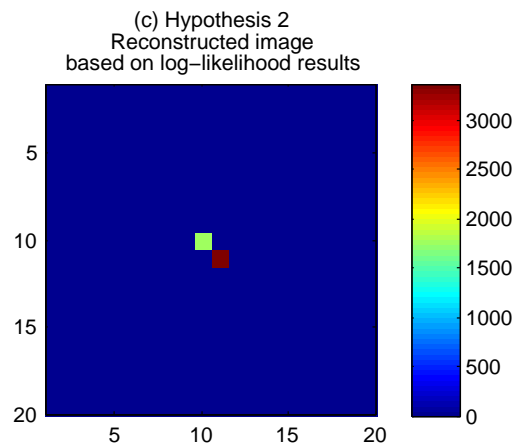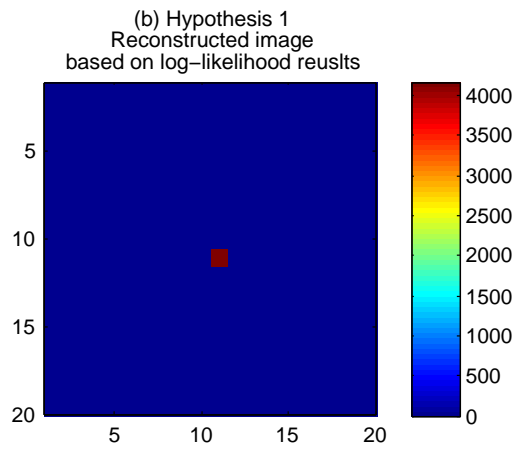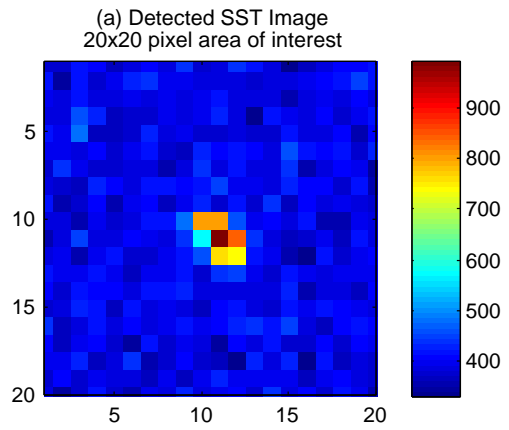
Figure 4.10: First measured image (a) Detected image, (b) Result of hypothesis one, (c) Result of hypothesis two. The log-likelihood of hypothesis two was larger and therefore a binary was detected.

4.3.3 Third image: two points touching.

The third frame in this sequence is a lot like the first, where there are clearly two binaries in the region of interest. The multi-hypothesis process correctly detected the binary.
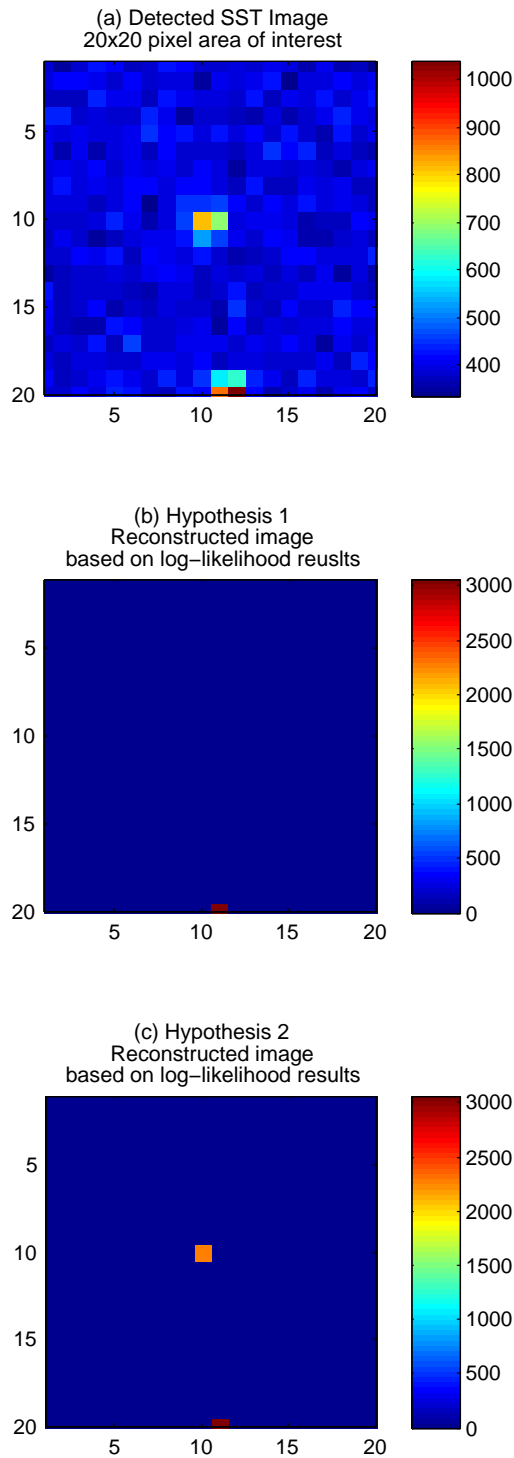
Figure 4.11: Third measured image (a) Detected image, (b) Result of hypothesis one, (c) Result of hypothesis two. The log-likelihood of hypothesis two was larger and therefore a binary was detected.

4.3.4 Fourth image: single point.

The last image in this sequence shows the star has passed out of the region of interest. Here log-likelihood for hypothesis one should be larger. The result of processing this image was the log-likelihood of hypothesis two did not detect any combination of two points that rose above the threshold for detection, so it remained defaulted to zero. Whereas the log-likelihood of hypothesis one correctly detected the single object.
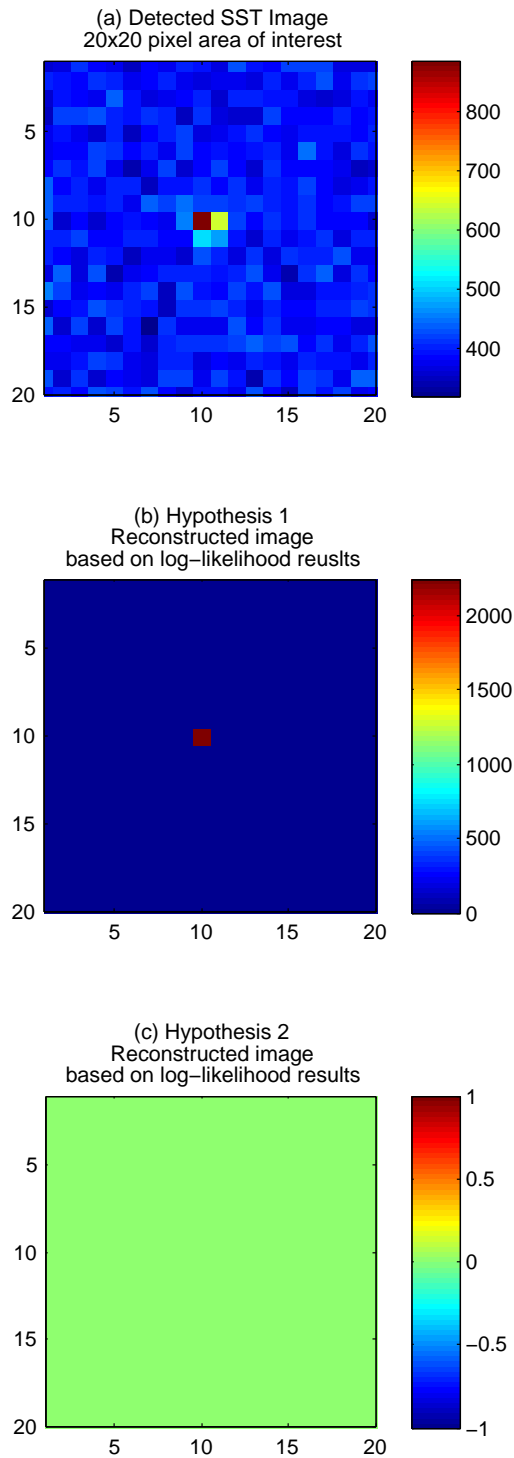
Figure 4.12: Forth measured image (a) Detected image, (b) Result of hypothesis one, (c) Result of hypothesis two. The log-likelihood of hypothesis one was greater and so a binary was not detected.

71

4.3.5 *Measured data result summary.*

These results demonstrate that the multi-hypothesis algorithm can properly differentiate between a single point source and a binary point source in the images shown above. The processing time on a laptop with two gigahertz processor running Matlab™was approximately six milliseconds per image. This also demonstrates the potential to run this detection algorithm in near-real-time to flag images with potential binaries in an area of interest. These flagged image locations can then be revisited by higher resolution imaging if desired.

V. Future work

5.1 Summary

Binary detection is an important area of interest both inside and outside the Air Force. Traditional binary detection at geosynchronous orbiting heights is difficult when objects are too close and/or blurred by atmospheric effects. Many post processing techniques have been implemented to enhance the resolution and thereby increase the ability to detect binaries. This thesis has proposed a different approach that focuses instead on assuming an image contains either zero, one, or two point sources. Based of these hypothesis a log-likelihood can be calculated which can be used for binary detection.

Chapter two reviewed current binary detection techniques along with a brief introduction about multi-hypothesis testing. Chapter three provided the derivations used in this thesis along with a description of the simulated and measured tests conducted. Chapter four provided the test results, comparing an imaging by correlation detection method with the multi-hypothesis algorithm.

Multi-hypothesis testing capitalizes on the additional data contained in the assumptions which form each hypothesis. This additional information allows the derivation of a binary detection algorithm with positive simulation results when compared with an imaging by correlation detection method. If an objective of an imaging system is to search for and identify binaries then implementing a multi-hypothesis algorithm can provide increased detection performance because of the additional information contained in the hypothesis.

5.2 Future work

This thesis focused on actual image data. An early objective that was not realized in this research was to use multi-hypothesis testing on the spatial frequency information. A unique cosine fringe pattern in the spatial frequency information of an image denotes

a binary is present. However, sometimes this cosine pattern cannot be seen. Deriving a multi-hypothesis algorithm that assumes the spatial frequency data was formed by zero, one, or two point sources could allow better detection than current methods.

Another area of more research is how well this method performs when using multi-frame imaging techniques. The simulation tests in this thesis used only single short exposure images. Given the positive performance from these short exposure tests does create a suspicion that multi-frame imaging techniques will only enhance the performance even more as noise and atmospheric effects are removed through averaging many frames.

Sub-pixel detection was also not explored. When viewing objects that fit inside a single pixel in the detection plane, if the object is not centered on the pixel it will split the photon count into two or more adjacent pixels. Adding a multi-hypothesis binary detection that accounts for sub-pixel locations is a potential area for more investigation.

In a similar vein, detection of more than two objects might be of interest. Having hypothesis calculations for zero, one, two, and more than two would allow not only binary but also cluster detection in a given area of interest. This is also an important part of the Air Force's mission for space surveillance.

Bibliography

[1] Acton, DS and RC Smithson. "Solar imaging with a segmented adaptive mirror". *Applied optics*, 31(16):3161–3169, 1992.

[2] Ayers, GR, MJ Northcott, and JC Dainty. "Knox-Thompson and triple-correlation imaging through atmpshperic turbulence". *JOSA A*, 5(7):963–985, 1988.

[3] Bates, RHT. "Astronomical speckle imaging". *Physics Reports*, 90(4):203–297, 1982.

[4] Beletic, James W. "Deterministic photon bias in speckle imaging". *Optics Communications*, 71(6):337–340, 1989.

[5] Campisi, Patrizio and Karen Egiazarian. *Blind image deconvolution: theory and applications*. CRC press, 2007.

[6] Charbonneau, David, Timothy M. Brown, David W. Latham, and MIchel Mayor. "Detection of Planetary Transits Across a Sun-like Star". 529(1):L45, 2000. URL http://stacks.iop.org/1538-4357/529/i=1/a=L45.

[7] Collins, Graham P. "Making stars to see stars: DOD adaptive optics work is declassified". *Physics Today*, 45:17, 1992.

[8] Ealey, Mark A. and John A. Wellman. "Deformable mirrors: design fundamentals, key performance specifications, and parametric trades". *San Diego-DL tentative*, 36–51. International Society for Optics and Photonics, 1992.

[9] Foy, R. and A. Labeyrie. "Letter to the Editor Feasibility of adaptive telescope with laser probe". *Astron. Astrophys*, 152:L29–L31, 1985.

[10] Fugate, Robert Q. "Laser beacon adaptive optics". *Optics and Photonics News*, 4(6):14–19, 1993.

[11] Gardner, Chester S., Byron M. Welsh, and Laird A. Thompson. "Design and performance analysis of adaptive optical telescopes using lasing guide stars". 78(11):1721–1743, 1990.

[12] Gaskill, Jack D. *Linear systems, Fourier transforms, and optics*. IET, 1978.

[13] Goodman, J. W. *Statistical Optics*. Wiley, John and Sons, Inc, New York, NY, 1985.

[14] Goodman, J. W. *Introduction to Fourier Optics*. Roberts and Company Publishers, Greenwood Village, CO, 2005.

[15] Happer, W., GJ MacDonald, CE Max, and FJ Dyson. "Atmospheric-turbulence compensation by resonant optical backscattering from the sodium layer in the upper atmosphere". *JOSA A*, 11(1):263–276, 1994.

[16] Hardy, John W. "Active optics: a new technology for the control of light". *Proceedings of the IEEE*, 66(6):651–697, 1978.

[17] Hulburd, Bill. "Segmented mirrors for atmospheric compensation". *1989 Intl Congress on Optical Science and Engineering*, 42–51. International Society for Optics and Photonics, 1989.

[18] Knox, Keith T. and Brian J. Thompson. "Recovery of images from atmospherically degraded short-exposure photographs". *The astrophysical journal*, 193:L45–L48, 1974.

[19] Kundur, Deepa and Dimitrios Hatzinakos. "Blind image deconvolution". *Signal Processing Magazine, IEEE*, 13(3):43–64, 1996.

[20] Labeyrie, Antoine. "Attainment of Diffraction Limited Resolution in Large Telescopes by Fourier Analysing Speckle Patterns in Star Images".

[21] Lawrence, TW, DM Goodman, EM Johansson, and JP Fitch. "Speckle imaging of satellites at the us air force maui optical station". *Applied optics*, 31(29):6307–6321, 1992.

[22] Lohmann, Adolf W., Gerd Weigelt, and Bernhard Wirnitzer. "Speckle masking in astronomy: triple correlation theory and applications". *Applied Optics*, 22(24):4028–4037, 1983.

[23] Marcy, Geoffrey W., R. Paul Butler, Debra Fischer, Steven S. Vogt, Jack J. Lissauer, and Eugenio J. Rivera. "A Pair of Resonant Planets Orbiting GJ 876". *The Astrophysical Journal*, 556(1):296, 2001. URL http://stacks.iop.org/0004-637X/556/i=1/a=296.

[24] Matson, Charles L. "Weighted-least-squares phase reconstruction from the bispectrum". *JOSA A*, 8(12):1905–1913, 1991.

[25] Meng, Julian, George JM Aitken, E. Keith Hege, and Jeffrey S. Morgan. "Triple-correlation subplane reconstruction of photon-address stellar images". *JOSA A*, 7(7):1243–1250, 1990.

[26] Northcott, MJ, GR Ayers, and JC Dainty. "Algorithms for image reconstruction from photon-limited data using the triple correlation". *JOSA A*, 5(7):986–992, 1988.

[27] Phillips, James D. and Stephen C. Cain. "Joint maximum likelihood estimator for pupil and image plane data". *Optical Engineering*, 47(2):026002–026002, 2008.

[28] Ribak, Erez N. "Deformable mirrors". *NATO ASI Series C Mathematical and Physical Sciences-Advanced Study Institute*, 423:149–162, 1994.

[29] Richmond, Richard D. and Stephen C. Cain. *Direct-detection LADAR systems*. SPIE Press, 2010.

[30] Roddier, Nicolas A. "Atmospheric wavefront simulation using Zernike polynomials". *Optical Engineering*, 29(10):1174–1180, 1990.

[31] Roggemann, M. C. and B. M. Welsh. *Imaging Through Turbulence*. CRC Press LLC, Boca Raton, FL, 1996.

[32] Rousset, Gerard. "Wave-front sensors". *Adaptive optics in astronomy*, 1:91, 1999.

[33] Schmidt, J. D. *Numerical Simulation of Optical Wave Propigation With examples in MATLAB©* . SPIE Press, Bellingham, WA, 2010.

[34] Schulz, T. J. and D. L. Snyder. "Image recovery from correlations". 1992.

[35] Schulz, Timothy J. "Multiframe blind deconvolution of astronomical images". *JOSA A*, 10(5):1064–1073, 1993.

[36] Schwartz, C., E. Ribak, and SG Lipson. "Bimorph adaptive mirrors and curvature sensing". *JOSA A*, 11(2):895–902, 1994.

[37] Thompson, Laird A. "Adaptive optics in astronomy". *Physics Today*, 47:24, 1994.

[38] Troxel, Steven E., Byron M. Welsh, and Michael C. Roggemann. "Off-axis optical transfer function calculations in an adaptive-optics system by means of a diffraction calculation for weak index fluctuations". *JOSA A*, 11(7):2100–2111, 1994.

[39] Troxel, Steven E., Byron M. Welsh, and Michael C. Roggemann. "Anisoplanatism effects on signal-to-noise ratio performance of adaptive optical systems". *JOSA A*, 12(3):570–577, 1995.

[40] Tyson, Robert. *Principles of adaptive optics*. CRC Press, 2010.

REPORT DOCUMENTATION PAGE

1. REPORT DATE *(DD–MM–YYYY)*	2. REPORT TYPE	3. DATES COVERED *(From — To)*
27–03–2014	Master's Thesis	Oct 2013–Mar 2014

4. TITLE AND SUBTITLE

Binary Detection using Multi-Hypothesis Log-Likelihood, Image Processing

5a. CONTRACT NUMBER

5b. GRANT NUMBER

5c. PROGRAM ELEMENT NUMBER

6. AUTHOR(S)

Gessel, Brent H., Captain, USAF

5d. PROJECT NUMBER

5e. TASK NUMBER

5f. WORK UNIT NUMBER

7. PERFORMING ORGANIZATION NAME(S) AND ADDRESS(ES)

Air Force Institute of Technology
Graduate School of Engineering and Management (AFIT/EN)
2950 Hobson Way
WPAFB, OH 45433-7765

8. PERFORMING ORGANIZATION REPORT NUMBER

AFIT-ENG-14-M-34

9. SPONSORING / MONITORING AGENCY NAME(S) AND ADDRESS(ES)

Lt Col Travis Blake
Space Systems (DARPA/TTO)
675 North Randolph Street
Arlington, VA 22203-2114
(703)812-1963

10. SPONSOR/MONITOR'S ACRONYM(S)

DARPA/TTO

11. SPONSOR/MONITOR'S REPORT NUMBER(S)

12. DISTRIBUTION / AVAILABILITY STATEMENT

DISTRIBUTION STATEMENT A:
APPROVED FOR PUBLIC RELEASE; DISTRIBUTION UNLIMITED

13. SUPPLEMENTARY NOTES

This work is declared a work of the U.S. Government and is not subject to copyright protection in the United States.

14. ABSTRACT

One of the United States Air Force missions is to track space objects. Finding planets, stars, and other natural and synthetic objects are all impacted by how well the tools of measurement can distinguish between these objects when they are in close proximity. In astronomy, the term *binary* commonly refers to two closely spaced objects. *Splitting* a binary occurs when two objects are successfully detected. The physics of light, atmospheric distortion, and measurement imperfections can make binary detection a challenge.

Binary detection using various post processing techniques can significantly increase the probability of detection. This paper explores the potential of using a multi-hypothesis approach. Each hypothesis assumes one two or no points exists in a given image. The log-likelihood of each hypothesis are compared to obtain detection results. Both simulated and measured data are used to demonstrate performance with various amounts of atmosphere, and signal to noise ratios. Initial results show a significant improvement when compared to a detection via imaging by correlation. More work exists to compare this technique to other binary detection algorithms and to explore cluster detection.

15. SUBJECT TERMS

binary detection, image post processing, correlation

16. SECURITY CLASSIFICATION OF:			17. LIMITATION OF ABSTRACT	18. NUMBER OF PAGES	19a. NAME OF RESPONSIBLE PERSON
a. REPORT	b. ABSTRACT	c. THIS PAGE			Dr. Stephen C. Cain (ENG)
U	U	U	UU	90	19b. TELEPHONE NUMBER *(include area code)* (937) 255-3636 x4716 Stephen.Cain@afit.edu